



THE UNIVERSITY *of* EDINBURGH

## Edinburgh Research Explorer

### **Deterministic numerical solutions of the Boltzmann equation using the fast spectral method**

**Citation for published version:**

Wu, L, White, C, Scanlon, TJ, Reese, JM & Zhang, Y 2013, 'Deterministic numerical solutions of the Boltzmann equation using the fast spectral method', *Journal of Computational Physics*, vol. 250, pp. 27-52.  
<https://doi.org/10.1016/j.jcp.2013.05.003>

**Digital Object Identifier (DOI):**

[10.1016/j.jcp.2013.05.003](https://doi.org/10.1016/j.jcp.2013.05.003)

**Link:**

[Link to publication record in Edinburgh Research Explorer](#)

**Document Version:**

Peer reviewed version

**Published In:**

Journal of Computational Physics

**General rights**

Copyright for the publications made accessible via the Edinburgh Research Explorer is retained by the author(s) and / or other copyright owners and it is a condition of accessing these publications that users recognise and abide by the legal requirements associated with these rights.

**Take down policy**

The University of Edinburgh has made every reasonable effort to ensure that Edinburgh Research Explorer content complies with UK legislation. If you believe that the public display of this file breaches copyright please contact [openaccess@ed.ac.uk](mailto:openaccess@ed.ac.uk) providing details, and we will remove access to the work immediately and investigate your claim.



# Deterministic numerical solutions of the space-inhomogeneous Boltzmann equation using the fast spectral method

Lei Wu, Craig White, Thomas J. Scanlon, Jason M. Reese and Yonghao Zhang

*James Weir Fluids Lab, Department of Mechanical and Aerospace Engineering, University of Strathclyde, Glasgow G1 1XJ, UK*

---

## Abstract

The Boltzmann equation describes the dynamics of rarefied gas flows, but the multidimensional nature of its collision operator poses a real challenge for its numerical solution. In this paper, the fast spectral method [33], originally developed by Mouhot and Pareschi for the numerical solutions of the collision operator, is extended to deal with other collision kernels, such as those corresponding to the soft, Lennard-Jones, and rigid attracting potentials. The accuracy of the fast spectral method is checked by comparing our numerical solutions of the space-homogeneous Boltzmann equation with the exact Bobylev-Krook-Wu solutions for a gas of Maxwell molecules. It is found that the accuracy is improved by replacing the trapezoidal rule with Gauss-Legendre quadrature in the calculation of the kernel mode, and the conservation of momentum and energy are ensured by the Lagrangian multiplier method without loss of spectral accuracy. The relax-to-equilibrium processes of different collision kernels with the same value of shear viscosity are then compared; the numerical results indicate that different forms of the collision kernels can be used as long as the shear viscosity (not only the value, but also its temperature dependence) is recovered. An iteration scheme, where the numerical errors decay exponentially, is employed to obtain stationary solutions of the space-inhomogeneous Boltzmann equation. Four classical benchmarking problems are investigated: the normal shock wave, and the planar Fourier/Couette/force-driven Poiseuille flows. For normal shock waves, our numerical results are compared with a finite difference solution of the Boltzmann equation for hard sphere molecules, experimental data, and molecular dynamics simulation of argon using the realistic Lennard-Jones potential. For planar Fourier/Couette/force-driven Poiseuille flows, our results are compared with the direct simulation Monte Carlo method. Excellent agreements are observed in all test cases, demonstrating the merit of the fast spectral method as a computationally efficient method for rarefied gas dynamics.

*Keywords:* Boltzmann equation, Lennard-Jones potential, Sutherland's formula of shear viscosity, Fourier spectral method, rarefied gas dynamics

---

## 1. Introduction

The fundamental task in the study of gas dynamics is to obtain the evolution of macroscopic quantities such as density, bulk velocity, temperature, pressure tensor, and heat flux. Only when the Knudsen number (the ratio of the molecular mean free path to a characteristic flow length, or characteristic flow frequency to mean collision frequency) is small, can the evolution of macroscopic quantities be governed by partial differential equations such as the Navier-Stokes-Fourier equations, Burnett equations, or the Grad-13 moment equations [1]. As the Knudsen number becomes appreciable, it is necessary to adopt microscopic descriptions. Since the gas consists of a large number of molecules, the Newtonian description is computationally unrealistic. So we turn to the Boltzmann equation under the assumptions of molecular chaos and binary collisions. It uses the one-particle distribution function to describe the system state, and macroscopic quantities are derived from the velocity moments of the distribution function. In Boltzmann's description, all molecules move in straight lines with fixed velocities until they encounter elastic collisions with other molecules. The collision is modelled by a nonlinear collision operator, where the interatomic potential is incorporated into the collision kernel. The structure of the collision operator is rather complicated: it is a fivefold integral with three dimensions in velocity space and two dimensions in a unit sphere.

The multidimensional structure of the collision operator poses a real challenge to the numerical solution of the Boltzmann equation. From a historical point of view, realistic numerical computations of the Boltzmann equation are based on probabilistic methods. Well-known examples are the direct simulation Monte Carlo (DSMC) methods developed by Bird and Nanbu [2, 3]. Despite their stochastic nature, DSMC solutions converge to those of the Boltzmann equation for a monatomic gas in the limit of vanishing discretization and stochastic errors [4]. The main advantages of the DSMC method are: (i) the simulated particles in DSMC represent a large number of real molecules so that the number of operations is greatly reduced; (ii) it does not need artificial boundaries in velocity space; (iii) particles concentrate in regions where the distribution function is not small so that computer memory is not wasted; (iv) it is very efficient for high-speed rarefied gas flows. However, DSMC becomes time-consuming if the flow is in the continuum-fluid regime, especially when the Mach number is small. Note that recently developed hybrid continuum/particle approaches [5, 6, 7, 8] and the variance reduced DSMC method [9, 10] have partly eased these difficulties.

Contrasting with the particle methods, there are numerical methods that solve the Boltzmann equation deterministically, including the discrete velocity model (DVM), the finite-difference method, and the Fourier spectral method. A brief introduction to these methods is given below.

In 1989, Goldstein, Sturtevant, and Broadwell developed the first version of DVM [11]. They used a fixed set of discrete velocities to approximate the continuous velocity space, and constructed a discrete collision mechanics on the velocity nodes in order to preserve the main physical properties of the collision operator. However, a large amount of computational resources are wasted since the post-collision velocities must lie on the velocity nodes. Bobylev,

Palczewski, and Schneider considered the direct approximation of the collision operator and demonstrated that the computational cost is of the order  $O(N^7)$ , while the formal accuracy is less than first order in velocity, where  $N$  is the number of grid points in each velocity direction [12]. The high computational cost drove researchers to consider mixed deterministic and stochastic methods [13, 14, 15]. Recently, Morris, Varghese, and Goldstein used an interpolation scheme to map the post-collision velocities back onto the velocity nodes and found that the performance of DVM is comparable to (or even faster than) DSMC in normal shock wave simulations [16, 17]. Also note that Mouhot, Pareschi, and Rey constructed a DVM for hard sphere molecules with computational cost  $O(\bar{N}^3 N^3 \log N)$ ,  $\bar{N} \ll N$  [18].

The kinetic theory group in Kyoto has developed a family of finite difference methods for the Boltzmann equation. In 1989, Sone, Ohwada, and Aoki proposed an accurate numerical kernel method for computing the linearized collision operator for hard sphere molecules [19]. Four years later, Ohwada extended the finite-difference method to calculate the full nonlinear collision operator for hard sphere molecules [20, 21]. This method seems to be restricted to one-dimensional problems such as normal shock flow and Fourier heat flow between two parallel plates where the velocity distribution function has a cylindrical symmetry, i.e., it is a function of the longitudinal and transversal velocities. In this way, the number of velocity nodes and the computational cost are dramatically reduced. In 2001, the finite difference method was applied by Kosuge, Aoki, and Takata to the Boltzmann equation for a binary gas mixture of hard sphere molecules [22].

In 1996, inspired by the pioneering work of Bobylev using Fourier transform techniques in the analysis of the Boltzmann equation for Maxwell molecules [23], Pareschi and Perthame proposed a spectral method to approximate the collision operator for a class of collision kernels, where the computational cost is of the order  $O(N^6)$  [24]. One year later, Bobylev and Rjasanow developed a numerical method to solve the collision operator for Maxwell molecules with computational cost of the order  $O(N^4)$  [25]. This is in general the fastest algorithm to date. However, its formal accuracy is only of the order  $O(N^{-1/2})$ . For one-dimensional problems such as Fourier heat flow and normal shock flow, Watchararuangwita, Grigoriev, and Meleshko observed that cylindrical symmetry allows a reduction of the computational cost to the order  $O(N^2 \log N)$  by employing the fast Fourier transform (FFT) in the longitudinal velocity direction and Hankel transform in the transverse direction [26]. In 1999, based on the Carleman representation, Bobylev and Rjasanow were able to solve the collision operator for hard sphere molecules with a computational cost  $O(N^6 \log N)$  and formal accuracy  $O(N^{-2})$ , using generalized Radon and X-ray transforms [27]. A faster numerical method with a computational cost  $O(N^6)$  and formal accuracy  $O(N^{-2})$  has also been proposed for the variable hard sphere (VHS) model by Ibragimov and Rjasanow [28]. Based on these Fourier spectral methods, Gamba and Tharkabhushanam developed a spectral-Lagrangian method both for elastic and inelastic collision operators and investigated space-inhomogeneous problems, i.e., one-dimensional Fourier heat flow and shock flow [29, 30].

In 2000, Pareschi and Russo developed an algorithm to solve the collision operator for the VHS model with a computational cost of  $O(N^6)$  [31]. The approximation of the collision operator is spectrally accurate for smooth velocity distribution functions, where the decay rate

of the error is faster than any polynomial, i.e., faster than  $O(N^{-r})$  for any  $r > 0$ . The method has been successfully applied to space-inhomogeneous problems in two-dimensional velocity space [32]. Six years later, by means of the Carleman-like representation, Mouhot and Pareschi developed a faster spectral algorithm with a computational cost  $O(M^2 N^3 \log N)$  and spectral accuracy, where  $M$  is the number of grid points in the discretizations of polar and azimuthal angles [33]. In practical calculations,  $M \ll N$ , say,  $M = 4 \sim 6$  [33, 34]. The fast spectral method has been applied to space-inhomogeneous problems in two-dimensional velocity space as well as quantum collision operators [34, 35, 36, 37]. Surprisingly, so far we have not seen any attempt to apply the fast spectral method to physically meaningful space-inhomogeneous problems in three-dimensional velocity space.

In terms of accuracy and computational cost, the fast spectral method seems to be the best one among all the Fourier spectral methods [33]. Compared to the VHS model where the collision kernel is isotropic (independent of the deflection angle), this algorithm works only for hard sphere molecules. However, by introducing special forms of anisotropic collision kernels, the fast spectral method can be extended to many intermolecular interaction models. This paper is devoted to the improvement and application of the fast spectral method in the following three ways:

1. Novel anisotropic collision kernels are designed, extending the applicability of the fast spectral method to all inverse power-law potentials except the Coulomb potential. Also, special collision kernels are designed for molecules interacting through the Lennard-Jones (LJ) potential and rigid attracting potential, by observing that cross-sections for these potentials can be approximated well by superpositions of several single-term cross-sections. Nevertheless, the numerical simulations are as fast as that for a single-term collision kernel.
2. In the calculation of the kernel mode, the integration in a unit sphere is approximated by the Gauss-Legendre quadrature, instead of the trapezoidal rule. Better accuracy is achieved for the same number of discrete polar and azimuthal angles.
3. Since the fast spectral method conserves mass and approximates momentum and energy with spectral accuracy, we use the method of Lagrangian multipliers to correct the momentum and energy. While it ensures conservation, the Lagrangian multiplier method does not affect the accuracy of the fast spectral method.

Our modified fast spectral method is then applied to space-inhomogeneous problems such as the normal shock wave and planar Fourier/Couette/force-driven Poiseuille flows. Its accuracy is checked by comparing numerical results with analytical solutions, experimental data, and other numerical results obtained from the finite-difference method, molecular dynamics (MD), and DSMC.

The rest of the paper is organized as follows. In Section 2, the problems are stated and the Boltzmann equation is introduced. We show how to recover the shear viscosity when special forms of the anisotropic collision kernels (especially the collision kernels for the realistic LJ potential and rigid attracting potential) are used. We normalize the Boltzmann equation and give the boundary conditions for the normal shock flow and planar

Fourier/Couette/force-driven Poiseuille flows. In Section 3, detailed calculation of the spectral approximation of the collision operator is presented, and the accuracy of the fast spectral method is checked by comparing the numerical results with analytical solutions for Maxwell molecules. The relax-to-equilibrium process of different collision kernels with the same value of shear viscosity is then compared in Section 4. An iteration scheme is used to find steady solutions of the space-inhomogeneous problems in Section 5. Various comparisons with the finite-difference method, experiment, MD, and DSMC are made for normal shock flows and planar Fourier/Couette/force-driven Poiseuille flows. Finally, in Section 6, we conclude with a summary of the proposed numerical method and future perspectives.

## 2. Formulation of problems

### 2.1. Fourier/Couette/force-driven Poiseuille flows and shock waves

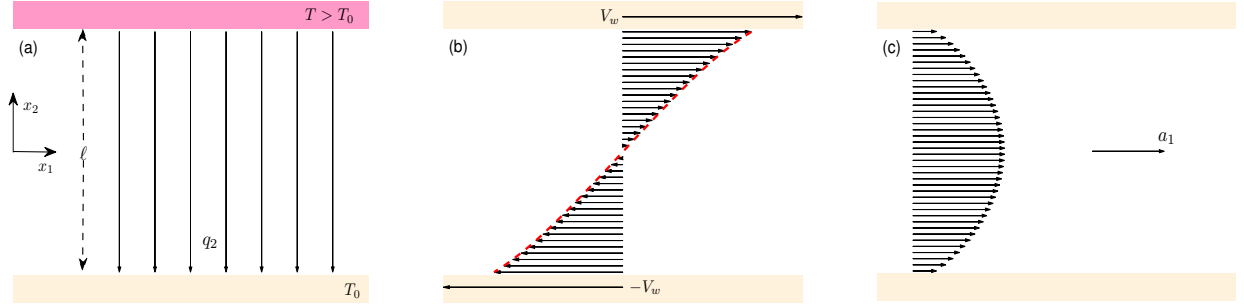


Figure 1: Sketch of (a) Fourier, (b) Couette, and (c) force-driven Poiseuille flows between parallel plates.

Consider a rarefied monatomic gas between two parallel infinite plates located at  $x_2 = \ell/2$  and  $x_2 = -\ell/2$ , where  $x = (x_1, x_2, x_3)$  is the rectangular space coordinate system. In Couette flow, the upper and lower plates move with velocity  $V_w$  and  $-V_w$  in the direction parallel to the plates (the  $x_1$  direction), while in Fourier and Poiseuille flows the plate velocities are zero (see Fig. 1). No pressure gradient exists in the  $x_1$  and  $x_3$  directions. No external force is exerted in the Couette and Fourier flows, but in the Poiseuille flow the gas is subject to a uniform external force in the  $x_1$  direction (the acceleration is denoted by  $a_1$ ). In the Couette and Poiseuille flows, the wall temperatures are kept at  $T_0$ , while in the Fourier flow the temperature of the upper wall is higher than that of the lower wall  $T_0$ . Maxwell's diffusive boundary condition is employed to account for the wall effects. When the average molecular number density  $n_0$  and the intermolecular potential are known, the stationary state will be uniquely determined. We then analyze the density, velocity, temperature, shear stress, and heat flux profiles of the steady Fourier/Couette/force-driven Poiseuille flows.

We also consider a planar shock wave perpendicular to the flow in the  $x_2$  direction. The flow is uniform at the upstream ( $x_2 = -\infty$ ) and downstream ( $x_2 = \infty$ ) ends. The upstream molecule number density, temperature, and Mach number are denoted by  $n_0$ ,  $T_0$ , and  $Ma$ , respectively, while those of the downstream end can be determined through the Rankine-Hugoniot relations. We are interested in the structure of the normal shock wave when the stationary state is reached.

## 2.2. Boltzmann equation

The state of a dilute monatomic gas is described by the distribution function  $f(t, x, v)$ , where  $t$  is the time and  $v = (v_1, v_2, v_3)$  is the molecular velocity. The distribution function is defined in such a way that the quantity  $f(t, x, v)dx dv$  is the particle number in the phase-space volume  $dx dv$ . All macroscopic quantities can then be calculated via the velocity moments of the distribution function: the molecular number density is  $n(t, x) = \int_{\mathbb{R}^3} f(t, x, v)dv$ , the bulk velocity is  $V(t, x) = \int_{\mathbb{R}^3} v f(t, x, v)dv/n(t, x)$ , the temperature is  $T(t, x) = m \int_{\mathbb{R}^3} |v - V|^2 f(t, x, v)dv/3k_B n(t, x)$ , the pressure tensor is  $P_{ij}(t, x) = m \int_{\mathbb{R}^3} (v_i - V_i)(v_j - V_j) f(t, x, v)dv$ , and the heat flux is  $q_i(t, x) = m \int_{\mathbb{R}^3} |v - V|^2 (v_i - V_i) f(t, x, v)dv/2$ , where  $m$  is the mass of a molecular,  $k_B$  is the Boltzmann constant, and the subscripts  $i, j$  denote the spatial directions.

For molecules undergoing binary elastic collisions, the evolution of the distribution function in the planar Fourier/Couette/force-driven Poiseuille flows and normal shock waves is governed by the following celebrated Boltzmann equation:

$$\frac{\partial f}{\partial t} + v_2 \frac{\partial f}{\partial x_2} + a_1 \frac{\partial f}{\partial v_1} = Q(f, f), \quad (1)$$

where  $Q(f, f)$  is the quadratic collision operator consisting of the gain term  $Q^+$  and the loss term  $Q^-$ . The collision operator is local in  $(t, x)$ . For simplicity the time and space position will be omitted in writing the collision operator

$$Q(f, f) = \underbrace{\int_{\mathbb{R}^3} \int_{\mathbb{S}^2} B(\cos \theta, |v - v_*|) f(v'_*) f(v') d\Omega dv_*}_{Q^+} - \underbrace{\nu(v) f(v)}_{Q^-}, \quad (2)$$

where

$$\nu(v) = \int_{\mathbb{R}^3} \int_{\mathbb{S}^2} B(\cos \theta, |v - v_*|) f(v_*) d\Omega dv_*, \quad (3)$$

is the collision frequency. Here  $v, v_*$  are the pre-collision particle velocities, while  $v', v'_*$  are the corresponding post-collision velocities. Conservation of momentum and energy yield the following relations

$$\begin{aligned} v' &= \frac{v + v_*}{2} + \frac{|v - v_*|}{2} \Omega = v + \frac{|u| \Omega - u}{2}, \\ v'_* &= \frac{v + v_*}{2} - \frac{|v - v_*|}{2} \Omega = v_* - \frac{|u| \Omega - u}{2}, \end{aligned} \quad (4)$$

where  $u = v - v_*$  is the relative pre-collision velocity and  $\Omega$  is a vector in the unit sphere  $\mathbb{S}^2$  along the relative post-collision velocity  $v' - v'_*$ . The deflection angle  $\theta$  between the pre- and post-collision relative velocities satisfies  $\cos \theta = \Omega \cdot u/|u|$ ,  $0 \leq \theta \leq \pi$ .

The collision kernel (probability)  $B(\cos \theta, |v - v_*|)$  is always non-negative, and depends on the modulus of the relative velocity and the deflection angle. For hard sphere molecules, the deflection angle is determined through  $b = d \cos(\theta/2)$ , where  $b$  is the aiming distance and  $d$  is the molecular diameter. Hence the differential cross-section  $\sigma = b|db|/\sin \theta |d\theta|$  is

$d^2/4$  and the collision kernel  $B = |u|\sigma$  is  $|u|d^2/4$ . For a general spherically symmetrical intermolecular potential  $\phi(r)$ , the deflection angle is (see [1], p.170; [2], p.37)

$$\theta(b, |u|) = \pi - 2 \int_0^{W_1} \left[ 1 - W^2 - \frac{4\phi(r)}{m|u|^2} \right]^{-1/2} dW, \quad (5)$$

where  $W = b/r$  and  $W_1$  is the positive root of the term in the brackets. Specifically, in the case of the  $(\eta - 1)$ -th inverse power-law potential<sup>1</sup>, the collision kernel is a power-law function of the relative velocity:

$$B = \frac{b|db|}{\sin \theta |d\theta|} |u| \equiv c_\alpha(\theta) |u|^\alpha, \quad \alpha = \frac{\eta - 5}{\eta - 1}. \quad (6)$$

At the grazing collision limit  $\theta \rightarrow 0$ ,  $c_\alpha(\theta) \sim \theta^{(\alpha-5)/2}$ , indicating that the total cross-section  $\int \sigma d\Omega$  is infinite. Although the global existence and rapid relax-to-equilibrium of the classical solutions has been proven [38], a finite cutoff is introduced in numerical simulations using particle methods such as DSMC and MD. One way to eliminate the infinity is to cut off the function  $c_\alpha(\theta)$ , i.e., set  $c_\alpha(\theta) = 0$  when  $\theta$  is smaller than a fixed value of angle, or equivalently, when  $b$  is larger than a fixed value of distance. This is justified by the fact that grazing collisions only lead to small changes of the system state. Another prevalent way to simplify the collision kernel is to replace  $c_\alpha(\theta)$  with the constant  $C_\alpha$ , yielding the well-known VHS model [2]:

$$B = C_\alpha |u|^\alpha, \quad (7)$$

where the constant  $C_\alpha$  is empirically determined by equating the shear viscosity coefficient of the Boltzmann equation when the collision kernel is given by Eq. (6) with that when the collision kernel is by Eq. (7). According to the Chapman-Enskog expansion [1], the shear viscosity is given by<sup>2</sup>

$$\mu = \frac{5\sqrt{\pi m k_B T}}{8D}, \quad D = \left( \frac{m}{4k_B T} \right)^4 \int_0^\infty u^7 \sigma_\mu \exp\left(-\frac{mu^2}{4k_B T}\right) du, \quad (8)$$

where  $\sigma_\mu = 2\pi \int_0^\pi \sigma \sin^3 \theta d\theta$  is the viscosity cross-section, we therefore have

$$C_\alpha = \frac{3}{4} \left( \frac{2\kappa}{m} \right)^{2/(\eta-1)} A_2(\eta), \quad (9)$$

with the numerical factor  $A_2(\eta) = \int_0^\infty \sin^2 \theta W_0 dW_0$  and  $W_0 = b(m|u|^2/2\kappa)^{1/(\eta-1)}$  [2]. Note that in the VHS model, the shear viscosity is

$$\mu \propto T^\omega, \quad \omega = \frac{\eta + 3}{2(\eta - 1)}. \quad (10)$$

---

<sup>1</sup>The potential is  $\phi(r) = \kappa/(\eta - 1)r^{\eta-1}$ , which is called hard and soft potentials when  $\eta > 5$  and  $\eta < 5$ , respectively; Maxwell molecules have the potential with  $\eta = 5$  and the Coulomb potential has  $\eta = 2$ .

<sup>2</sup>Only the first-order term of the Sonine-polynomials is used to calculate the shear viscosity [1], as the rest of the terms are negligible. For example, they make zero contribution to the shear viscosity for Maxwell molecules, and only make a 2% contribution for hard sphere molecules.



In the VHS model, the differential cross-section  $\sigma = C_\alpha |u|^{\alpha-1}$  is independent of the deflection angle. This model is widely used in DSMC, and the isotropic cross-section makes DSMC easy and effective to implement when  $\alpha \geq 0$ . For other numerical methods to solve the collision operator efficiently, it may be easier to include the  $\theta$ -dependent collision kernel and the total cross-section does not have to be finite. For example, Mouhot and Pareschi [33] suggested the following anisotropic collision kernel:

$$B = C'_\alpha \sin^{\alpha-1} \left( \frac{\theta}{2} \right) |u|^\alpha, \quad (11)$$

where  $C'_\alpha$  is a constant. This special  $\theta$ -dependent collision kernel not only enables the development of the fast spectral algorithm for computing the collision operator deterministically, but also mimics the growth trend of the collision kernel when decreasing the deflection angle. Similarly, the constant  $C'_\alpha$  is determined by equating the shear viscosity coefficient of the Boltzmann equation when the collision kernel is given by Eq. (6) with that when the collision kernel is given by Eq. (11), yielding

$$C'_\alpha = \frac{(\alpha+3)(\alpha+5)}{24} C_\alpha. \quad (12)$$

Note that for hard sphere molecules ( $\alpha = 1$ ), the VHS collision kernel and the collision kernel (11) are exactly the same.

We find that the collision kernel (11) can be extended to the following general form:

$$B = C''_{\alpha,\gamma} \sin^{\alpha+\gamma-1} \left( \frac{\theta}{2} \right) \cos^{-\gamma} \left( \frac{\theta}{2} \right) |u|^\alpha, \\ C''_{\alpha,\gamma} = \frac{\Gamma[(7+\alpha)/2]}{6\Gamma[(3+\alpha+\gamma)/2]\Gamma(2-\gamma/2)} C_\alpha, \quad (13)$$

where  $\Gamma$  is the gamma function. The additional parameter  $\gamma$  introduces plenty of flexibility to not only extend the applicability of the fast spectral method to all inverse power-law potentials except the Coulomb potential, but also to recover the correct ratio between coefficients of shear viscosity and diffusion.

### 2.3. Lennard-Jones potential

The power-law intermolecular potential is a phenomenological model. In reality, the potential between monatomic gas molecules is better described by the LJ potential. Here we consider argon, where the LJ potential is

$$\phi(r) = 4\epsilon \left[ \left( \frac{d_{LJ}}{r} \right)^{12} - \left( \frac{d_{LJ}}{r} \right)^6 \right], \quad (14)$$

with a potential depth  $\epsilon = 119.18k_B$ ,  $d_{LJ} = 3.42 \times 10^{-10}m$ , and  $r$  being the distance between two molecules. For other molecules, the values of  $\epsilon$  and  $d_{LJ}$  may be different. However, the following analysis applies to all LJ potentials of the form in Eq. (14).

Unlike the power-law potential, the shear viscosity is not a single power-law function of the temperature over the whole temperature range [1]. Only when the temperature does not vary too much could  $D$  be a single power-law function of  $T$ . For instance, when  $k_B T/\epsilon$  is large (or small), the repulsive (or attractive) part of the force is dominant, and  $D \propto T^{-1/6}$  (or  $D \propto T^{-1/3}$ ). Also, when  $2 < k_B T/\epsilon < 3$ , we have  $D \propto T^{-0.31}$ , see Fig. 2. In these regions, the VHS model can be successfully implemented in DSMC, producing satisfactory results. However, a single power-law fit is not adequate over a wider temperature range. To tackle this problem, the generalized VHS model of Hassan and Hash [39], the variable sphere model of Matsumoto [40], and the generalized soft sphere model of Fan [41], have been proposed and tested in DSMC.

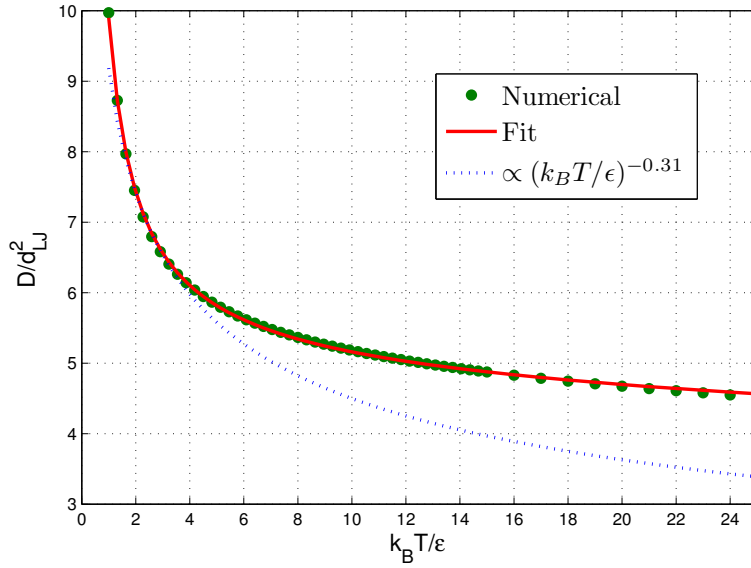


Figure 2:  $D/d_{LJ}^2$  vs  $k_B T/\epsilon$  for the LJ potential, see Eq. (8). The solid line is a nonlinear least squares fit (with 95% confidence bounds) of  $D/d_{LJ}^2$  as a function of  $k_B T/\epsilon$  by the sum of three power-law functions:  $D/d_{LJ}^2 = b_1(k_B T/\epsilon)^{-0.4} + b_2(k_B T/\epsilon)^{-0.45} + b_3(k_B T/\epsilon)^{-0.5}$ , with  $b_1 = 407.4$ ,  $b_2 = -811.9$ , and  $b_3 = 414.4$ .

Here we employ the concept of the generalized VHS model to construct the collision kernel that is suitable for the fast spectral method to solve the collision operator. According to Eq. (8), we observe that the special form of  $D$  given by the fit function in Fig. 2 can be recovered if the collision kernel takes the form of

$$B = \frac{d_{LJ}^2}{32\pi} \sum_{j=1}^3 \frac{(m/4\epsilon)^{(\alpha_j-1)/2} b_j}{\Gamma(\frac{3+\alpha_j}{2})} \sin^{\alpha_j-1} \left( \frac{\theta}{2} \right) |u|^{\alpha_j}, \quad (15)$$

where  $\alpha_1 = 0.2$ ,  $\alpha_2 = 0.1$ ,  $\alpha_3 = 0$ , and the values of  $b_j$  are shown in Fig. 2.

For argon with  $\epsilon = 119.18 k_B$ , the fit in Fig. 2 covers the temperature range from 120K to 3000K, while the VHS model with  $\mu \propto T^{0.81}$  (dotted line) works only when  $240\text{K} < T < 360\text{K}$ . For wider temperature range, more terms with different values of  $\alpha_j$  may be needed. We note that, no matter how many terms are added, the computational efficiency of the corresponding

collision operator will not increase. The reason for this will be discussed in Section 3. In the following, if the LJ potential is not specified, the shear viscosity of argon is proportional to  $T^{0.81}$ , that is, the collision kernel is given by Eq. (11) or Eq. (13) with  $\alpha = 0.38$ .

#### 2.4. Sutherland's molecular model

For a gas whose molecules are rigid attracting spheres, its shear viscosity is given by the Sutherland formula:

$$\mu = \frac{5\sqrt{\pi m k_B T}}{16\sigma_{T,\infty}} \frac{T}{T + T_s}, \quad (16)$$

where  $T_s$  is a reference temperature and  $\sigma_{T,\infty}$  is the total cross-section in the limiting case of infinite relative velocity  $|u|$ . This formula reproduces the experimental data for many real gases over a considerable range of temperature [1, 2].

The Sutherland formula for shear viscosity can be recovered if we use the following superposition of the modified collision kernels

$$B = C''_{1,\gamma_1} \sin^{\gamma_1} \left( \frac{\theta}{2} \right) \cos^{-\gamma_1} \left( \frac{\theta}{2} \right) |u| + C''_{-1,\gamma_2} \sin^{\gamma_2-2} \left( \frac{\theta}{2} \right) \cos^{-\gamma_2} \left( \frac{\theta}{2} \right) |u|^{-1}, \quad (17)$$

with

$$\begin{aligned} 8\pi C''_{1,\gamma_1} \Gamma \left( 2 - \frac{\gamma_1}{2} \right) \Gamma \left( 2 + \frac{\gamma_1}{2} \right) &= 2\sigma_{T,\infty}, \\ 8\pi C''_{-1,\gamma_2} \Gamma \left( 2 - \frac{\gamma_2}{2} \right) \Gamma \left( 1 + \frac{\gamma_2}{2} \right) &= 2\sigma_{T,\infty} T_s \frac{4k_B}{m}, \end{aligned} \quad (18)$$

where special values of  $\gamma_1$  and  $\gamma_2$ , i.e.,  $2 > \gamma_1 = \gamma_2 > 0$ , can make the fast spectral method as fast as that for the single-term collision kernel (11) or (13). Detailed discussions will be given in Section 3.

#### 2.5. Normalization

For practical calculations, it is convenient and useful to use dimensionless variables. The following dimensionless variables are introduced for the planar Fourier/Couette/force-driven Poiseuille flows:

$$\begin{aligned} \tilde{f} &= \frac{v_m^3}{n_0} f, \quad \tilde{x} = \frac{x}{\ell}, \quad (\tilde{v}, \tilde{V}, \tilde{V}_w) = \frac{(v, V, V_w)}{v_m}, \\ \tilde{t} &= \frac{v_m}{\ell} t, \quad \tilde{a}_1 = \frac{\ell}{v_m^2} a_1, \quad \tilde{n} = \frac{n}{n_0}, \quad \tilde{T} = \frac{T}{T_0}, \\ \tilde{P}_{ij} &= \frac{P_{ij}}{n_0 k_B T_0}, \quad \tilde{q} = \frac{q}{n_0 k_B T_0 v_m}, \end{aligned} \quad (19)$$

where  $n_0$  is the average molecular number density, and  $v_m = \sqrt{2k_B T_0/m}$  is the most probable molecular speed. In the simulation of shock waves, the normalization is exactly the same, except the  $\ell$  is then related to the mean free path in the upstream end, instead of the distance between two parallel plates.

The Boltzmann equation with the collision kernel (13) becomes

$$\frac{\partial \tilde{f}}{\partial t} + \tilde{v}_2 \frac{\partial \tilde{f}}{\partial \tilde{x}_2} + \tilde{a}_1 \frac{\partial \tilde{f}}{\partial \tilde{v}_1} = \frac{1}{Kn'} \int \int \sin^{\alpha+\gamma-1} \left( \frac{\theta}{2} \right) \cos^{-\gamma} \left( \frac{\theta}{2} \right) |\tilde{u}|^\alpha [\tilde{f}(\tilde{v}_*) \tilde{f}(\tilde{v}') - \tilde{f}(\tilde{v}_*) \tilde{f}(\tilde{v})] d\Omega d\tilde{v}_*, \quad (20)$$

where

$$Kn' = \frac{64\sqrt{2}^\alpha}{5} \Gamma \left( \frac{\alpha + \gamma + 3}{2} \right) \Gamma \left( 2 - \frac{\gamma}{2} \right) Kn, \quad (21)$$

with

$$Kn = \frac{\mu(T = T_0)}{n_0 \ell} \sqrt{\frac{\pi}{2mk_B T_0}} \quad (22)$$

being the unconfined Knudsen number, where  $[\mu(T = T_0)/n_0] \sqrt{\pi/2mk_B T_0}$  is the unconfined mean free path at the reference temperature  $T_0$ . Note that the unconfined mean free-path is  $15\pi/2(7 - 2\omega)(5 - 2\omega)$  times larger than the equilibrium mean free path defined in Eq. (4.52) in Ref. [2].

For the LJ potential, when the collision kernel takes the form of Eq. (15), the term  $\sin^{\alpha+\gamma-1}(\theta/2) \cos^{-\gamma}(\theta/2) |\tilde{u}|^\alpha / Kn'$  in Eq. (20) should be replaced by

$$\frac{5 \sum_{j=1}^3 b_j (k_B T_0 / 2\epsilon)^{(\alpha_j-1)/2} \sin^{\alpha_j-1}(\theta/2) |\tilde{u}|^{\alpha_j} / \Gamma(\frac{\alpha_j+3}{2})}{64\sqrt{2}Kn \sum_{j=1}^3 a_j (k_B T_0 / \epsilon)^{(\alpha_j-1)/2}}. \quad (23)$$

A similar expression can be given for the rigid attracting potential.

Considering the above normalization scheme, the normalized macroscopic quantities are related to the normalized distribution function as follows:

$$\begin{aligned} \tilde{n} &= \int \tilde{f} d\tilde{v}, \quad \tilde{V} = \frac{1}{\tilde{n}} \int \tilde{v} \tilde{f} d\tilde{v}, \quad \tilde{T} = \frac{2}{3\tilde{n}} \int |\tilde{v} - \tilde{V}|^2 \tilde{f} d\tilde{v}, \\ \tilde{P}_{ij} &= 2 \int (\tilde{v}_i - \tilde{V}_i)(\tilde{v}_j - \tilde{V}_j) \tilde{f} d\tilde{v}, \quad \tilde{q}_i = \int |\tilde{v} - \tilde{V}|^2 (\tilde{v}_i - \tilde{V}_i) \tilde{f} d\tilde{v}. \end{aligned} \quad (24)$$

## 2.6. Boundary conditions

In the planar Couette and Poiseuille flows, the symmetry of the problems with respect to the  $\tilde{x}_2$  axis allows us to consider only half of the spatial region  $-1/2 \leq \tilde{x}_2 \leq 0$ . At the lower plate, according to Maxwell's diffusive boundary condition, the distribution function for the reflected particles is given by:

$$\begin{aligned} \tilde{f} &= \frac{\tilde{n}}{\pi^{3/2}} \exp[-(\tilde{v}_1 + \tilde{V}_w)^2 - \tilde{v}_2^2 - \tilde{v}_3^2], \quad \text{for } \tilde{v}_2 \leq 0, \\ \tilde{n} &= 2\sqrt{\pi} \int_{\tilde{v}_2 < 0} \tilde{v}_2 \tilde{f}(\tilde{x}_2 = -0.5, \tilde{v}) d\tilde{v}, \end{aligned} \quad (25)$$

while in the middle between the two plates, we have  $\tilde{f}(\tilde{v}_1, \tilde{v}_2, \tilde{v}_3) = \tilde{f}(-\tilde{v}_1, -\tilde{v}_2, \tilde{v}_3)$  for Couette flow and  $\tilde{f}(\tilde{v}_1, \tilde{v}_2, \tilde{v}_3) = \tilde{f}(\tilde{v}_1, -\tilde{v}_2, \tilde{v}_3)$  for Poiseuille flow.

For planar Fourier flow, however, we do not have this kind of symmetry. The boundary condition at the lower plate is the same as Eq. (25) with  $\tilde{V}_w = 0$ , while that at the upper plate is

$$\begin{aligned}\tilde{f} &= \frac{\tilde{n}}{(\pi T_r)^{3/2}} \exp\left(-\frac{\tilde{v}_1^2 + \tilde{v}_2^2 + \tilde{v}_3^2}{T_r}\right), \quad \text{for } \tilde{v}_2 < 0, \\ \tilde{n} &= 2\sqrt{\frac{\pi}{T_r}} \int_{\tilde{v}_2 > 0} \tilde{v}_2 \tilde{f}(\tilde{x}_2 = 0.5, \tilde{v}) d\tilde{v},\end{aligned}\tag{26}$$

where  $T_r$  is the temperature ratio of the upper and lower plates.

For shock waves, the distribution function at the upstream end is

$$\tilde{f} = \frac{1}{\pi^{3/2}} \exp\left[-\tilde{v}_1^2 - (\tilde{v}_2 - \sqrt{\frac{5}{6}}Ma)^2 - \tilde{v}_3^2\right],\tag{27}$$

and that at the downstream end is

$$\tilde{f} = \frac{n_d}{(\pi T_d)^{3/2}} \exp\left[-\frac{\tilde{v}_1^2 + (\tilde{v}_2 - V_d)^2 + \tilde{v}_3^2}{T_d}\right],\tag{28}$$

where, according to the Rankine-Hugoniot relations, we have the following molecular number density, bulk velocity, and temperature at the downstream end:

$$\begin{aligned}n_d &= \frac{4Ma^2}{Ma^2 + 3}, \\ V_d &= \sqrt{\frac{5}{96}} \frac{Ma^2 + 3}{Ma}, \\ T_d &= \frac{(5Ma^2 - 1)(Ma^2 + 3)}{16Ma^2}.\end{aligned}\tag{29}$$

### 3. Deterministic numerical method

#### 3.1. Fast spectral method for the collision operator

The numerical approximation of the Boltzmann collision operator by the fast spectral method is now introduced and discussed. For its main properties we refer to the original papers [33, 34]. Some detailed calculations are presented below because different sources in the literature give different results for the kernel mode [33, 34, 37]. For simplicity, the tildes on normalized quantities will be omitted hereafter. We first consider the simple case where the collision kernel is given by Eq. (13).

We rewrite the collision operator using the Carleman-like representation. With the basic identity  $2 \int_{\mathbb{R}^3} \delta(2y \cdot u + |y|^2) f(y) dy = |u| \int_{\mathbb{S}^2} f(|u|\Omega - u) d\Omega$ , where  $\delta$  is Dirac's delta function,

the collision operator on the right hand side of Eq. (20) can be rewritten as

$$\begin{aligned}
Q(f, f) &= \frac{1}{Kn'} \int_{\mathbb{R}^3} \int_{\mathbb{S}^2} \Theta |u| [f(v'_*) f(v') - f(v_*) f(v)] d\Omega dv_* \\
&= \frac{1}{Kn'} \int_{\mathbb{R}^3} \int_{\mathbb{S}^2} \Theta |u| \left[ f\left(v_* - \frac{|u|\Omega - u}{2}\right) f\left(v + \frac{|u|\Omega - u}{2}\right) - f(v_*) f(v) \right] d\Omega dv_* \\
&= \frac{2}{Kn'} \int_{\mathbb{R}^3} \int_{\mathbb{R}^3} \Theta \delta(2y \cdot u + |y|^2) \left[ f\left(v_* - \frac{y}{2}\right) f\left(v + \frac{y}{2}\right) - f(v_*) f(v) \right] dy dv_* \\
&= \frac{4}{Kn'} \int_{\mathbb{R}^3} \int_{\mathbb{R}^3} \Theta \delta(y \cdot u + |y|^2) [f(v_* - y) f(v + y) - f(v_*) f(v)] dy dv_* \\
&= \frac{4}{Kn'} \int_{\mathbb{R}^3} \int_{\mathbb{R}^3} \Theta \delta(y \cdot z) [f(v + z) f(v + y) - f(v + y + z) f(v)] dy dz,
\end{aligned}$$

where  $\Theta = \sin^{\alpha+\gamma-1}(\theta/2) \cos^{-\gamma}(\theta/2) |u|^{\alpha-1}$ .

Notice that in the above calculations we have used the transformations  $y = (|u|\Omega - u)/2$  and  $z = v_* - v - y = -u - y$ . Therefore, the deflection angle  $\theta$  satisfies

$$\cos \theta = \frac{\Omega \cdot u}{|u|} = \frac{-(y - z) \cdot (y + z)}{|y + z|^2} \stackrel{y \perp z}{=} \frac{|z|^2 - |y|^2}{|y|^2 + |z|^2},$$

which results in  $\sin(\theta/2) = |y|/\sqrt{|y|^2 + |z|^2}$  and  $\cos(\theta/2) = |z|/\sqrt{|y|^2 + |z|^2}$ . Hence  $\Theta = |y|^{\alpha+\gamma-1}|z|^{-\gamma}$  and the collision operator is simplified to

$$Q(f, f) = \frac{4}{Kn'} \int_{\mathbb{R}^3} \int_{\mathbb{R}^3} \delta(y \cdot z) |y|^{\alpha+\gamma-1} |z|^{-\gamma} [f(v + z) f(v + y) - f(v + y + z) f(v)] dy dz. \quad (30)$$

In the fast spectral method, the distribution function is periodized on the velocity domain  $\mathcal{D}_L = [-L, L]^3$ . Here we adopt uniform grid points in velocity space:  $v_k(j_k) = 2j_k L/N_k$  with  $k = 1, 2, 3$ , where  $j_k \in [-N_k/2, -N_k/2 + 1, \dots, N_k/2 - 1]$  and  $N_k$  is the number of velocity grid points in the  $k$ -th velocity direction. Suppose  $\mathcal{B}_S$ , a sphere of radius  $S$  centered at the origin, is the support of the distribution function. Usually the minimum  $L = (3 + \sqrt{2})S/2$  is chosen to avoid the aliasing error caused by the periodicity of the velocity distribution function [31]. The distribution function is then approximated by a truncated Fourier series,

$$f(v) = \sum_{j=-(N_1, N_2, N_3)/2}^{(N_1, N_2, N_3)/2-1} \hat{f}_j \exp(i\xi_j \cdot v), \quad (31)$$

$$\hat{f}_j = \frac{1}{(2L)^3} \int_{\mathcal{D}_L} f(v) \exp(-i\xi_j \cdot v) dv, \quad (32)$$

where  $j = (j_1, j_2, j_3)$ ,  $i$  is the imaginary unit, and  $\xi_j = j\pi/L$  are the frequency components. Meanwhile, the collision operator (30) is truncated to  $Q(f, f) = 4 \int_{\mathcal{B}_R} \int_{\mathcal{B}_R} \delta(y \cdot z) |y|^{\alpha+\gamma-1} |z|^{-\gamma} [f(v + z) f(v + y) - f(v + y + z) f(v)] dy dz / Kn'$ , where  $R \geq \sqrt{2}S$  [33, 34]. Numerical analysis reveals that, however,  $R$  cannot be larger than  $L$ .

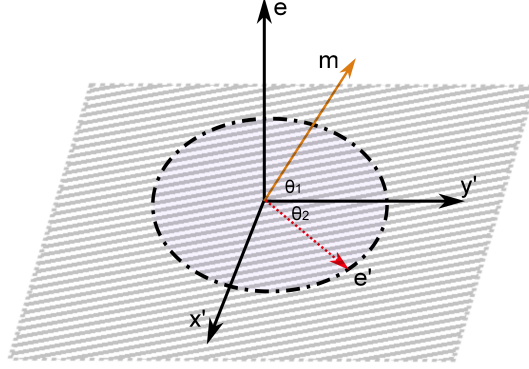


Figure 3: Demonstration of the integral with respect to  $e'$  used in the calculation of the kernel mode (34). When the vector  $e$  is fixed,  $e'$  is in the  $x'y'$  plane perpendicular to  $e$ . That is, it degenerates to a two-dimensional vector with  $\theta_2$  varying from 0 to  $2\pi$ . Because of symmetry, we only consider the region  $0 \leq \theta_2 \leq \pi$ .

Expanding also the truncated collision operator in the truncated Fourier series, we find that the  $j$ -th mode of the truncated collision operator is related to the Fourier coefficient  $\hat{f}$  of the distribution function:

$$\hat{Q}_j = \sum_{\substack{l+m=j \\ l,m=-(N_1,N_2,N_3)/2}}^{(N_1,N_2,N_3)/2-1} \hat{f}_l \hat{f}_m [\beta(l, m) - \beta(m, m)], \quad (33)$$

where  $l = (l_1, l_2, l_3)$ ,  $m = (m_1, m_2, m_3)$ , and the kernel mode  $\beta(l, m)$  is

$$\begin{aligned} \beta(l, m) &= \frac{4}{Kn'} \int_{\mathcal{B}_R} \int_{\mathcal{B}_R} \delta(y \cdot z) |y|^{\alpha+\gamma-1} |z|^{-\gamma} \exp(i\xi_l \cdot y + i\xi_m \cdot z) dy dz \\ &= \frac{1}{Kn'} \int \int \delta(e \cdot e') \left[ \int_{-R}^R |\rho|^{\alpha+\gamma} \exp(i\rho\xi_l \cdot e) d\rho \right] \left[ \int_{-R}^R |\rho'|^{1-\gamma} \exp(i\rho'\xi_m \cdot e') d\rho' \right] de' de \\ &= \frac{1}{Kn'} \int_{\mathbb{S}^2} \phi_{\alpha+\gamma}(\xi_l \cdot e) \left[ \int_{\mathbb{S}^2} \delta(e \cdot e') \phi_{1-\gamma}(\xi_m \cdot e') de' \right] de, \end{aligned} \quad (34)$$

with  $e, e'$  being the vectors in the unit sphere  $\mathbb{S}^2$ , and

$$\phi_\delta(s) = 2 \int_0^R \rho^\delta \cos(\rho s) d\rho. \quad (35)$$

Equation (34) can be simplified further. We construct a new Cartesian coordinate system, where the  $z'$  axis is parallel to the vector  $e$ , the  $y'$  axis is just the projection of vector  $m$  into the plane  $e_\perp$  perpendicular to the  $z'$  axis, and the  $x'$  axis is in the plane  $e_\perp$  and perpendicular to the  $y'$  axis, see Fig. 3. Suppose the polar and azimuthal angles of  $e'$  in the new coordinate system are  $\theta$  and  $\pi/2 - \theta_2$ , respectively, and the angle between the vector  $m$  and  $y'$ -axis is  $\theta_1$ . Then, we have  $\delta(e \cdot e') = \delta(\cos \theta)$  such that  $\int_0^\pi g(\theta) \delta(\cos \theta) d\theta = g(\pi/2)$  for arbitrary

function  $g(\theta)$ ,  $\xi_m \cdot e' = |\xi_m| \cos \theta_1 \cos \theta_2$ , and

$$\begin{aligned}\beta(l, m) &= \frac{1}{Kn'} \int_{S^2} \phi_{\alpha+\gamma}(\xi_l \cdot e) \left[ \int_0^{2\pi} \int_0^\pi \delta(\cos \theta) \phi_{1-\gamma}(|\xi_m| \cos \theta_1 \cos \theta_2) d\theta d\theta_2 \right] de \\ &= \frac{1}{Kn'} \int_{S^2} \phi_{\alpha+\gamma}(\xi_l \cdot e) \left[ \int_0^{2\pi} \phi_{1-\gamma}(|\xi_m| \cos \theta_1 \cos \theta_2) d\theta_2 \right] de \\ &= \frac{2}{Kn'} \int_{S^2} \phi_{\alpha+\gamma}(\xi_l \cdot e) \cdot \psi_\gamma(|\xi_m| \cos \theta_1) de,\end{aligned}\quad (36)$$

where

$$\psi_\gamma(s) = \int_0^\pi \phi_{1-\gamma}(s \cos \theta_2) d\theta_2 = 2\pi \int_0^R \rho^{1-\gamma} J_0(\rho s) d\rho, \quad (37)$$

with  $J_0$  being the zeroth-order Bessel functions.

Note that  $\xi_l (= l\pi/L)$  and  $\xi_m (= m\pi/L)$  in the integration (36) appear in two functions. If they appear also in two different functions in the final form of  $\beta(l, m)$ , Eq. (33) can be calculated effectively by the FFT-based convolution. The separation of  $l$  and  $m$  can be realized by calculating (36) approximately using the numerical quadrature method. Two different methods will be employed and compared:

- in the first method,  $\beta(l, m)$  is calculated numerically in spherical coordinates by the trapezoidal rule. Suppose the polar and azimuthal angles of the unit vector  $e$  are  $\theta$  and  $\varphi$ , respectively. We divide each region  $0 \leq \theta \leq \pi$  and  $0 \leq \varphi \leq \pi$  (for symmetry) into  $M$  sections, i.e.,  $\theta_p = p\pi/M$  and  $\varphi_q = q\pi/M$  with  $p, q = 1, 2, \dots, M$ . Then the kernel mode (36) is approximated by

$$\beta(l, m) \simeq \frac{4\pi^2}{Kn'M^2} \sum_{p,q=1}^{M-1,M} \phi_{\alpha+\gamma}(\xi_l \cdot e_{\theta_p, \varphi_q}) \cdot \psi_\gamma \left\{ \sqrt{|\xi_m|^2 - [\xi_m \cdot e_{\theta_p, \varphi_q}]^2} \right\} \cdot \sin \theta_p, \quad (38)$$

where  $e_{\theta_p, \varphi_q} = (\sin \theta_p \cos \varphi_q, \sin \theta_p \sin \varphi_q, \cos \theta_p)$ .

- in the second method,  $\beta(l, m)$  is approximated by a Gauss-Legendre quadrature of order  $M$ :

$$\beta(l, m) \simeq \frac{4}{Kn'} \sum_{p,q=1}^M \omega_p \omega_q \phi_{\alpha+\gamma}(\xi_l \cdot e_{\theta_p, \varphi_q}) \cdot \psi_\gamma \left\{ \sqrt{|\xi_m|^2 - [\xi_m \cdot e_{\theta_p, \varphi_q}]^2} \right\} \cdot \sin \theta_p, \quad (39)$$

where  $\theta_p$  ( $\varphi_q$ ) and  $\omega_p$  ( $\omega_q$ ) are the  $p$  ( $q$ )-th point and weight in the Gauss-Legendre quadrature with  $\theta, \varphi \in [0, \pi]$ .

For the LJ potential, when the normalized collision kernel is given by Eq. (23),  $\gamma$  is zero. Meanwhile, one needs to replace the term  $\phi_{\alpha+\gamma}(\xi_l \cdot e_{\theta_p, \varphi_q})/Kn'$  in Eq. (38) or Eq. (39) by

$$\frac{5 \sum_{j=1}^3 b_j (k_B T_0 / 2\epsilon)^{(\alpha_j-1)/2} \phi_{\alpha_j}(\xi_l \cdot e_{\theta_p, \varphi_q}) / \Gamma(\frac{\alpha_j+3}{2})}{64\sqrt{2}Kn \sum_{j=1}^3 a_j (k_B T_0 / \epsilon)^{(\alpha_j-1)/2}}. \quad (40)$$



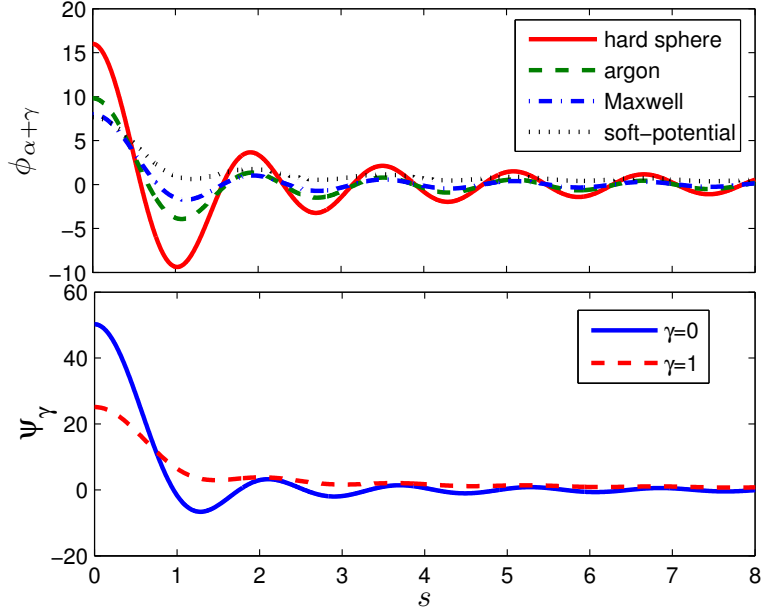


Figure 4: Profiles of  $\phi_{\alpha+\gamma}$  when  $\gamma = 0$  and  $\psi_\gamma$  according to Eqs. (35) and (37) when  $R = 4$ . Because of symmetry, the region  $s < 0$  is not plotted. For argon with a shear viscosity  $\mu$  proportional to  $T^{0.81}$ ,  $\alpha = 0.38$ , while for the soft potential, we use  $\alpha = -0.4$  and the shear viscosity is proportional to  $T^{1.2}$ .

The analytical form of  $\phi_{\alpha+\gamma}(s)$  can be obtained when  $\alpha + \gamma$  is an integer. For instance, when  $\gamma = 0$ , for Maxwell molecules ( $\alpha = 0$ ) and hard sphere molecules, we have

$$\begin{aligned}\phi_0(s) &= \frac{2 \sin(Rs)}{s}, \\ \phi_1(s) &= \frac{2R \sin(Rs)}{s} - \frac{4 \sin^2(Rs/2)}{s^2},\end{aligned}\tag{41}$$

while in the other cases,  $\phi_{\alpha+\gamma}(s)$  and  $\psi_\gamma(s)$  can be calculated by Gauss-Legendre quadrature numerically. Note that in the VHS model,  $-3 < \alpha \leq 1$ . From Eq. (35) it follows that  $\delta$  is restricted to the region  $(-1, +\infty)$ . Therefore,  $\alpha + \gamma > -1$  and  $1 - \gamma > -1$ . In the original collision kernel proposed by Mouhot and Pareschi [33],  $\gamma = 0$ , so that  $\alpha$  is restricted to the region  $(-1, 1]$ . This means that the original collision kernel cannot deal with general forms of soft potentials. In our modified collision kernel (13), if we let  $\gamma \rightarrow 2$ ,  $\alpha$  can cover the whole region  $(-3, 1]$ , thus extending the applicability of the fast spectral method to all inverse power-law potentials except the Coulomb potential. Fig. 4 shows typical decaying-oscillating profiles of the two functions  $\phi_{\alpha+\gamma}$  and  $\psi_\gamma$ , where we see the quasi-period of the oscillation is about  $2\pi/R$ .

### 3.2. Detailed implementation

The detailed procedure to approximate the collision operator is now outlined. In the following, we assume Eq. (36) is approximated by the trapezoidal rule. First, the kernel modes should be pre-computed and stored. The storage of  $\phi_{\alpha+\gamma}(\xi_l, \theta_p, \varphi_q)$  and  $\psi_\gamma(\xi_m, \theta_p, \varphi_q)$

requires  $2M(M-1)N_1N_2N_3$  units of compute memory. We also need  $N_1N_2N_3$  units of storage for

$$\phi_{loss} = \sum_{p,q=1}^{M-1,M} \phi_{\alpha+\gamma}(\xi_m, \theta_p, \varphi_q) \psi_\gamma(\xi_m, \theta_p, \varphi_q) \sin \theta_p, \quad (42)$$

which will be used to calculate the loss part of the collision operator. For space-homogeneous problems, such storage is relatively large when compared to the storage of the distribution function. However, when it comes to space-inhomogeneous problems, the storage will be relatively small because different locations could use the same kernel modes. Second, we get  $\hat{f}$  by applying the inverse FFT to  $f$ , see Step 1 in algorithm 1 in the Appendix. Third, with Eq. (38), Eq. (33) becomes

$$\begin{aligned} \hat{Q}_j \approx & \underbrace{\frac{4\pi^2}{Kn'M^2} \sum_{p,q=1}^{M-1,M} \sum_{\substack{l+m=j \\ l,m=-(N_1,N_2,N_3)/2}}^{(N_1,N_2,N_3)/2-1} [\hat{f}_l \phi_{\alpha+\gamma}(\xi_l, \theta_p, \varphi_q)] \cdot [\hat{f}_m \psi_\gamma(\xi_m, \theta_p, \varphi_q)]}_{\text{gain}} \\ & - \underbrace{\frac{4\pi^2}{Kn'M^2} \sum_{\substack{l+m=j \\ l,m=-(N_1,N_2,N_3)/2}}^{(N_1,N_2,N_3)/2-1} \hat{f}_l \cdot [\hat{f}_m \phi_{loss}]}_{\text{loss}}. \end{aligned} \quad (43)$$

The loss term can be effectively calculated by FFT-based convolution, using the zero-padding technique [42]. For the gain term, one has to do an FFT-based convolution for each pair of  $(p, q)$ . The implementation is listed in Steps 2, 3, and 4 in algorithm 1. Finally, the collision operator  $Q$  is calculated by applying FFT to  $\hat{Q}$  (Step 5).

Note that in algorithm 1, the zero-padding technique is employed to eliminate the aliasing error in the FFT-based convolution. This process is accurate for arbitrary values of  $t_1$  and  $t_2$  when the padding size in each direction is larger than one half of the velocity grid number. Considering the fact that the spectrum  $\hat{f}$  is non-zero only in the central region of the frequency domain, we can expedite the calculation by ignoring the zero-padding. This leads to the simpler and faster algorithm 2. Numerical simulations on Test 1 below show that both algorithms produce identical results, but algorithm 2 is about 4 times faster than algorithm 1.

Now we see that the computational cost of the fast spectral method is  $O(M^2N^3 \log N)$ , where  $N$  is the same order as  $N_1, N_2$  and  $N_3$ . Note that  $l$  and  $m$  are not separable in classical spectral methods, and the computational cost of Eq. (33) is  $O(N^6)$  [28, 29, 31]. A rough estimate of the speed-up can be given. In algorithm 2, one needs to do  $2M(M-1)+2$  times FFT (the array size is  $N_1 \times N_2 \times N_3$ ), while in classical spectral methods the computational cost is the same with one direct convolution of one complex and one real array of size  $N_1 \times N_2 \times N_3$ . For comparison, we take  $M = 7$  and run our Matlab (version 2012a) programs on a PC with an Intel Xeon 3.3 GHz CPU. For  $N = 32$  (or 64), algorithm 2 is about 18 (or 62) times faster than the classical spectral methods. Further speed-up can be

achieved by reducing the value of  $M$  (say, to 5) and considering possible symmetry in the distribution function.

Note that for the LJ potential, the storage of the kernel modes and computational cost of the collision operator is exactly the same as that for the single-term collision kernel (11) or (13). For the collision kernel (17), if we let  $\gamma_1 = \gamma_2$ , the storage and computational cost will also be the same as the single-term collision kernel. For the existence of  $\phi_{1+\gamma_1}$ ,  $\psi_{1-\gamma_1}$ ,  $\phi_{-1+\gamma_2}$ , and  $\psi_{1-\gamma_2}$ , one should choose  $-2 < \gamma_1 < 2$  and  $0 < \gamma_2 < 2$ . Therefore, we choose  $0 < \gamma_1 = \gamma_2 < 2$ . Note, if  $\gamma_1 \neq \gamma_2$ , the storage and computational cost will be twice that of the single-term collision kernel.

### 3.3. Conservation

One of the drawbacks of the fast spectral method, as with any spectral method for the approximation of the collision operator, is that it does not exactly conserve momentum and energy. To ensure the conservation of momentum and energy, we employ the method of Lagrangian multipliers [29, 30]. The procedure is simple and straightforward: after  $Q$  is obtained, we construct  $Q^{new}$  by minimizing the function  $\sum_j (Q_j - Q_j^{new})^2$  under the constraints  $\sum_j Q_j^{new} = \sum_j v_j Q_j^{new} = \sum_j |v_j|^2 Q_j^{new} = 0$ , yielding

$$Q_j^{new} = Q_j - (\lambda_n + \lambda_v \cdot v_j + \lambda_e |v_j|^2), \quad (44)$$

where the five Lagrangian multipliers satisfy

$$\begin{aligned} \sum_j Q_j &= \sum_j (\lambda_n + \lambda_v \cdot v_j + \lambda_e |v_j|^2), \\ \sum_j v_j Q_j &= \sum_j v_j (\lambda_n + \lambda_v \cdot v_j + \lambda_e |v_j|^2), \\ \sum_j |v_j|^2 Q_j &= \sum_j |v_j|^2 (\lambda_n + \lambda_v \cdot v_j + \lambda_e |v_j|^2). \end{aligned} \quad (45)$$

Since the errors for the momentum and energy in the fast spectral method are spectrally small [33], the Lagrangian multipliers are very small. This is indeed confirmed in our numerical simulations. We also find that the Lagrangian multiplier method does not affect the accuracy of the fast spectral method, while it ensures conservation of mass, momentum, and energy.

### 3.4. Accuracy of the fast spectral method

To check the accuracy of the fast spectral method, the relax-to-equilibrium process of spatially-homogeneous Maxwell molecules ( $\alpha, \gamma = 0$ ) is considered. The Boltzmann equation in this case becomes

$$\frac{\partial f}{\partial t} = \frac{1}{Kn'} \int_{\mathbb{R}^3} \int_{\mathbb{S}^2} \sin^{-1} \left( \frac{\theta}{2} \right) [f(v'_*)f(v') - f(v_*)f(v)] d\Omega dv_*, \quad (46)$$

where, without loss of generality, we choose  $Kn' = 32\pi/5$ .

Table 1: Relative error  $\sum_j |Q_j^{nu} - Q_j^{an}| / \sum_j |Q_j^{an}|$  in the approximation of the Boltzmann collision operator. T (G) stands for the trapezoidal rule (Gauss-Legendre quadrature) used in the approximation of Eq. (36). Parameters are  $L = 8$  and  $R = 6$ .

N		$M = 5$	6	7	8	12	16
16	T	4.58E-1	4.73E-1	4.55E-1	4.52E-1	4.78E-1	4.83E-1
	G	2.10E-1	3.35E-1	2.48E-1	2.77E-1	2.74E-1	2.69E-1
24	T	7.94E-2	5.20E-2	4.73E-2	3.93E-2	2.92E-2	2.59E-2
	G	4.61E-2	2.09E-2	9.16E-3	2.10E-2	1.72E-2	1.37E-2
32	T	5.54E-2	3.51E-2	2.57E-2	1.93E-2	8.39E-3	4.75E-3
	G	4.26E-2	6.18E-3	6.49E-4	2.11E-4	1.86E-4	1.57E-4
48	T	4.26E-2	3.88E-2	2.77E-2	2.08E-2	8.99E-3	5.01E-3
	G	4.31E-2	6.17E-3	6.09E-4	4.56E-5	4.94E-6	3.85E-6
64	T	5.90E-2	3.87E-2	2.77E-2	2.08E-2	8.99E-3	5.02E-3
	G	4.30E-2	6.16E-3	6.10E-4	4.70E-5	3.87E-6	4.31E-6

**Test 1.** The space-homogeneous Boltzmann equation (46) possesses the exact Bobylev-Krook-Wu (BKW) solution [43]:

$$f(v, t) = \frac{1}{2(2\pi K)^{3/2}} \exp\left(-\frac{|v|^2}{2K}\right) \left(\frac{5K-3}{K} + \frac{1-K}{K^2}|v|^2\right), \quad (47)$$

where the “effective temperature” is  $K = 1 - 0.4 \exp(-t/6)$ ,  $t \geq 0$ . According to the exact solution, the evolution of the fourth- and sixth-order moments is given by

$$\begin{aligned} M_4 &= \int f v_1^4 dv = 6K - 3K^2, \\ M_6 &= \int f v_1^6 dv = 45K^2 - 30K^3. \end{aligned} \quad (48)$$

The integration of Eq. (46) with respect to  $t$  will introduce some numerical error. In order to check how accurately the fast spectral method approximates the collision operator, we compare  $Q^{nu}$ , the numerical approximation of  $Q$ , to the analytical solution  $Q^{an}$ , which is calculated by  $Q^{an} = [f(t = \Delta t) - f(t = 0)]/\Delta t$  with the time step  $\Delta t = 1.0\text{E-}5$  far smaller than the characteristic relaxation time. The following two factors affect the accuracy: the value of  $N$ , which decides the accuracy of the spectrum  $\hat{f}$  of the distribution function, and the value of  $M$ , which determines how accurately we approximate the integral in Eq. (36). The latter is qualitatively analyzed as follows. For simplicity, let us ignore  $\xi_m$  and  $\varphi_\gamma$  in Eq. (36). Notice that  $\phi_{\alpha+\gamma}$  is a decaying-oscillating function with the quasi-period  $2\pi/R$  (see Eq. (41) and Fig. 4). Then, for a fixed value of  $\xi_l$ , the integral kernel in Eq. (36) oscillates  $R|\xi_l|/\pi$  times as  $\theta$  varies from 0 to  $\pi$ . In the worst cases ( $\xi_l \rightarrow N\pi/2L$ ), it oscillates  $O(N)$  times. This implies that  $M$  should be  $O(N)$ . In practical calculations, however,  $M$  can be far less than  $N$  because, if the distribution function has a support  $S$ , its spectrum has a

support proportional to  $1/S \sim 1/R$ . Within this support, the integral kernel in Eq. (36) oscillates only a few times, and hence a small value of  $M$  can lead to accurate results.

We vary values of  $N$  and  $M$  to see their influence on the numerical accuracy; the results are tabulated in Table 1. When  $N = 16$ , the relative error is large because the resolution of the distribution function is not high enough so that a large error exists in the spectrum  $\hat{f}$ . As  $N$  increases to 24, the error is reduced by one order of magnitude. When the trapezoidal rule is used, the error mainly comes from the approximation of Eq. (36), which decays at  $O(M^{-2})$  when  $N$  is fixed. When  $M$  is fixed, the numerical accuracy does not improve when  $N \geq 32$ . If we increase the value of  $M$  by a factor of 2 when the value of  $N$  is increased by a factor of 2, we come to the conclusion that when  $N \geq 32$ , roughly speaking, the accuracy of the fast spectral method is about  $O(N^{-2})$ , which is actually not spectrally accurate but has the same accuracy as the classical spectral methods [28, 29]. However, when Eq. (36) is approximated by the Gauss-Legendre quadrature, the spectral accuracy is clear for  $N \leq 32$  and  $M \geq 6$ . For  $N > 32$ , if  $M$  is increased linearly as the increase of  $N$ , spectral accuracy is maintained. For example, if we choose the minimum error between  $6 \leq M \leq 12$  for each  $N$ , the order of accuracy is 8.1 when  $N$  increases from 16 to 24; 13.5 when  $N$  increases from 24 to 32; and 8.9 when  $N$  increases from 32 to 48. Thus, in general, the approximation of Eq. (36) by Gauss-Legendre quadrature is better than that by the trapezoidal rule.

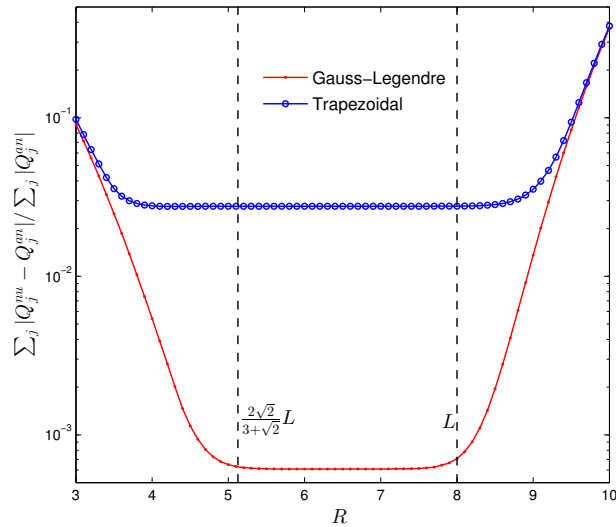


Figure 5: The relative error  $\sum_j |Q_j^{nu} - Q_j^{an}| / \sum_j |Q_j^{an}|$  as a function of  $R$ . Parameters are  $L = 8$ ,  $N = 48$ , and  $M = 7$ . Gauss-Legendre quadrature is used in the approximation of the kernel mode.

We now fix values of  $N$  and  $M$  to check the influence of  $R$  on the accuracy. Clearly, Fig. 5 indicates that  $R$  cannot be smaller than  $2\sqrt{2}L/(3 + \sqrt{2})$ , which is roughly  $\sqrt{2}$  times the support of the distribution function; otherwise, some collisions will be ignored in the truncated collision operator. Also,  $R$  cannot be larger than the size of the velocity domain, otherwise the aliasing error may destroy accuracy.

Next, we demonstrate the accuracy of the fast spectral method as a function of time, where Eq. (46) is solved by the Euler forward method with a time step of 0.001 (the time

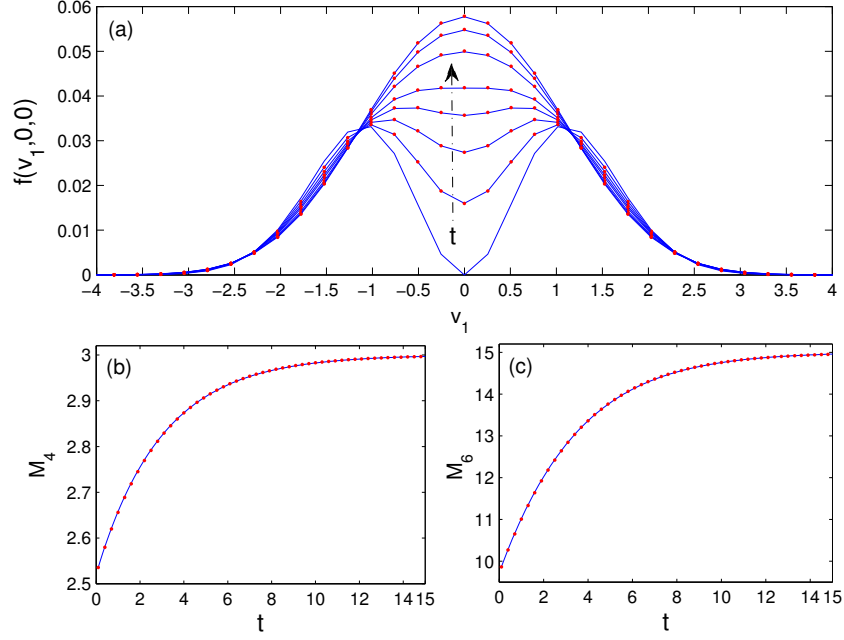


Figure 6: (a) Evolution of the distribution function  $f(v_1, 0, 0)$  of space-homogeneous Maxwell molecules, where the initial condition is given by Eq. (47). From bottom to top (near  $v_1 = 0$ ), the time corresponding to each line is 0, 0.5, 1, 1.5, 2, 3, 4, and 5. (b) and (c) Evolution of the fourth- and sixth-order moments, respectively. The solid lines represent the numerical results, while the dots are analytical predictions. The following parameters are used in the numerical simulation:  $L = 8$ ,  $R = 6$ ,  $N = 64$ , and  $M = 5$  with Eq. (38).

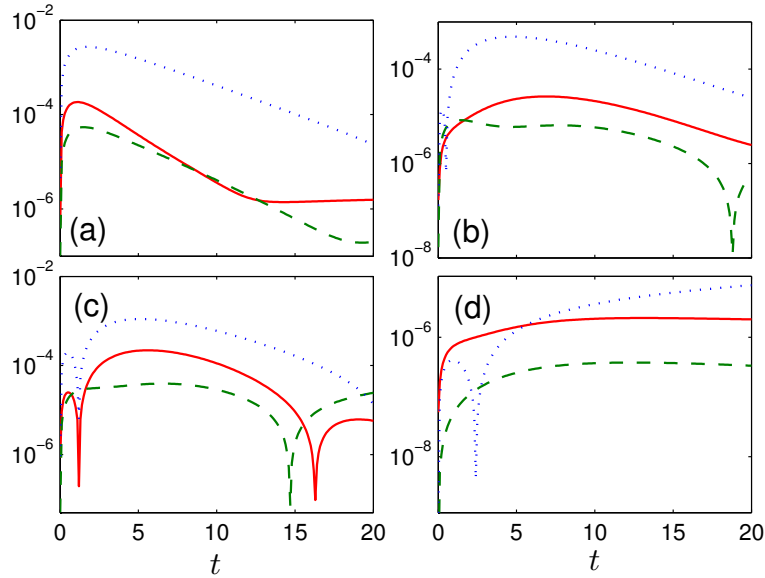


Figure 7: (a) Error  $(\sum_j |f^{nu} - f|^2 / \sum_j |f|^2)^{1/2}$  in the distribution function, (b) error in the fourth-order moment  $|M_4^{nu} - M_4|/M_4$ , (c) error in the sixth-order moment  $|M_6^{nu} - M_6|/M_6$ , and (d) error in the energy  $|(P_{xx}^{nu} + P_{yy}^{nu} + P_{zz}^{nu})/6 - 1|$  vs time. The solid and dashed lines are the results using Eq. (39) with  $N = 24$  and  $N = 32$ , respectively, while the dotted lines are the results using Eq. (38) with  $N = 32$ . Other parameters are  $L = 8$ ,  $R = 6$ , and  $M = 7$ .

step is far smaller than the characteristic relaxation time). Fig. 6 depicts the evolution of the distribution function, and the fourth- and sixth-order moments. Excellent agreement is found between the numerical and BKW solutions, even when Eq. (36) is approximated by the trapezoidal rule with  $M = 5$ . Fig. 7 shows the numerical errors in the distribution function, the fourth- and sixth-order moments, and energy as functions of time. It can be seen that when Eq. (36) is approximated by Gauss-Legendre quadrature, the numerical error with  $N = 32$  is one order of magnitude smaller than that with  $N = 24$ . Also, the accuracy of the results with  $N = 24$  is even better than that with  $N = 32$  when Eq. (36) is approximated by the trapezoidal rule. These results agree with what we found in Table 1. Furthermore, we find that the use of the Lagrangian method does not affect the numerical accuracy. This could be explained as follows: from Fig. 7(a) and (d) we see that the error in energy is far smaller than the error in the distribution function. Therefore, the correction in Eq. (44) has negligible influence on the distribution function but ensures conservation. Comparing the kernel mode (38) with those in Refs. [33, 34, 37], the term  $\sin \theta_p$  is missed in Refs. [33, 34] and an additional term  $\sin \theta_2$  is added in Eq. (37) in Ref. [37]. We have carried out numerical simulations using these kernel modes and found that none of them can accurately capture the evolution of the distribution function.

**Test 2.** For general forms of the initial distribution function, we cannot get the exact distribution functions. However, we know the exact evolution of its velocity moments. For example, when the initial distribution function takes the form

$$f(v, t=0) = \frac{1}{2(2\pi)^{3/2}} \exp\left(-\frac{|v - V_1|^2}{2}\right) + \frac{1}{2(2\pi)^{3/2}} \exp\left(-\frac{|v - V_2|^2}{2}\right), \quad (49)$$

with  $V_1 = (-2, 2, 0)$  and  $V_2 = (2, 0, 0)$ , the exact evolution of the pressure tensor is [29, 43]

$$\begin{aligned} P_{xx} &= \frac{14}{3} \exp\left(-\frac{t}{2}\right) + \frac{16}{3}, & P_{yy} &= -\frac{4}{3} \exp\left(-\frac{t}{2}\right) + \frac{16}{3}, \\ P_{zz} &= -\frac{10}{3} \exp\left(-\frac{t}{2}\right) + \frac{16}{3}, & P_{xy} &= -4 \exp\left(-\frac{t}{2}\right), \end{aligned} \quad (50)$$

and the exact evolution of the third-order moments is

$$\begin{aligned} r_x &= \int f v_1 |v|^2 dv = -4 \exp\left(-\frac{t}{2}\right), \\ r_y &= \int f v_2 |v|^2 dv = -\frac{4}{3} \exp\left(-\frac{t}{2}\right) + \frac{43}{3}. \end{aligned} \quad (51)$$

Figure 8 compares the evolution of the second- and third-order moments. It demonstrates that our numerical simulation produces accurate results when compared to the analytical ones given by Eqs. (50) and (51). From Fig. 9, the relative errors in  $P_{xx}$ ,  $P_{yy}$ , and  $r_y$  are about  $10^{-4}$ , while the errors are about  $10^{-5}$  when Eq. (36) is approximated by Gauss-Legendre quadrature. It is worthwhile to note that the spectral-Lagrangian method [29] cannot recover the third-order moments even when  $N = 40$ . Is this because the spectral-Lagrangian method is not spectrally accurate? We think that this is due to the integration

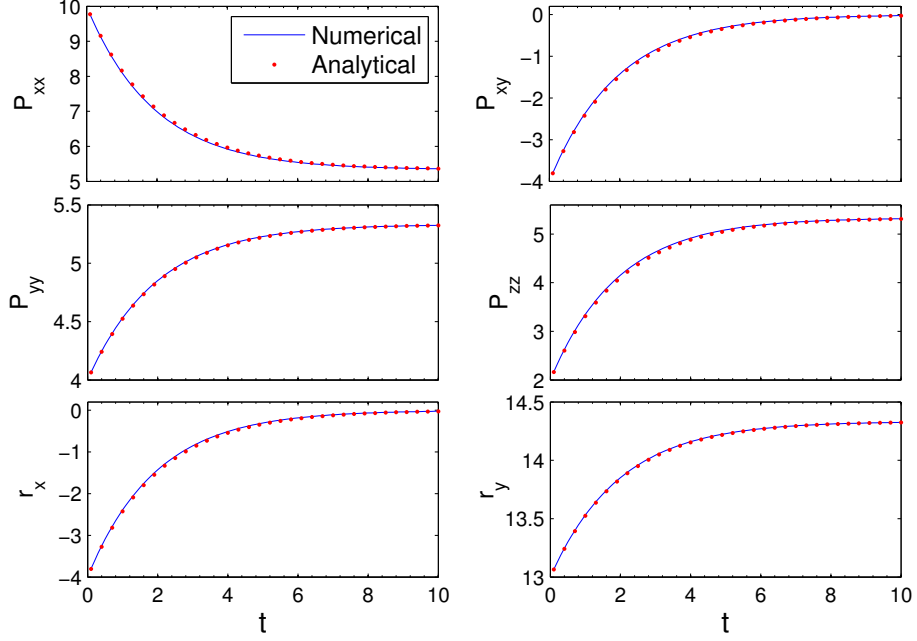


Figure 8: Evolution of the second- and third-order moments for space-homogeneous Maxwell molecules, where the initial distribution function is given by Eq. (49). The following parameters are used in the numerical simulation:  $L = 12$ ,  $R = 10$ ,  $N = 32$ , and  $M = 5$  with Eq. (38).

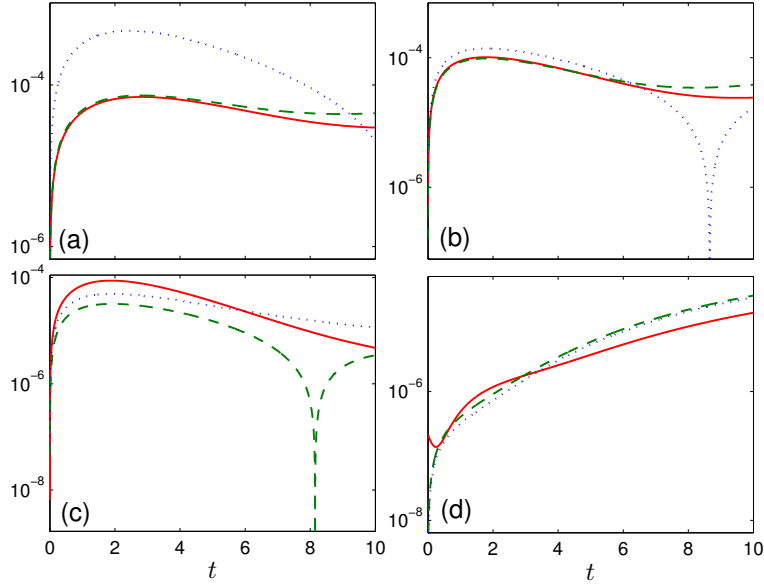


Figure 9: (a) Relative error  $|P_{xx}^{nu} - P_{xx}|/P_{xx}$ , (b) relative error  $|P_{yy}^{nu} - P_{yy}|/P_{yy}$ , (c) relative error  $|r_y^{nu} - r_y|/r_y$ , and (d) error in the energy  $|(P_{xx}^{nu} + P_{yy}^{nu} + P_{zz}^{nu})/16 - 1|$  vs time. The solid and dashed lines are the results using Eq. (39) when  $N = 24$  and  $N = 32$ , respectively, while the dotted lines are the results using Eq. (38) when  $N = 32$ . Other parameters are  $L = 12$ ,  $R = 10$ , and  $M = 7$ .



region given in Eq. (2.29) of Ref. [29] (which is related to the parameter  $R$  in the fast spectral method) being too large, so a significant aliasing error is introduced (see Fig. 5). Indeed, we find in our simulations that  $r_x$  and  $r_y$  deviate from the analytical solutions when  $R$  is outside the velocity domain.

**Test 3.** Notice that the initial distribution functions used in the two test cases above are smooth, and the spectral accuracy of the Fourier spectral method has been proven [33]. Now we consider the case where the initial distribution function is not smooth; it has a abrupt jump at  $v_1 = 0$ :

$$f(v, t = 0) = \frac{1}{3(2\pi)^{3/2}} \begin{cases} 4 \exp\left(-\frac{|v|^2}{2}\right), & v_1 \geq 0, \\ \exp\left(-\frac{v_1^2}{8} - \frac{v_2^2 + v_3^2}{2}\right), & v_1 < 0. \end{cases} \quad (52)$$

It can be shown analytically that the evolution of the second- and fourth-order moments is given by

$$\begin{aligned} P_{xx} &= \frac{4}{3} \exp\left(-\frac{t}{2}\right) + \frac{8}{3}, & P_{yy} &= -\frac{2}{3} \exp\left(-\frac{t}{2}\right) + \frac{8}{3}, \\ M'_4 &= \int f|v|^4 dv = \frac{22}{3} \exp\left(-\frac{t}{3}\right) + \frac{80}{3}. \end{aligned} \quad (53)$$

Figure 10 demonstrates that the fast spectral method can accurately capture the evolution of the second- and fourth-order moments, even when the initial distribution function has a large jump at  $v_1 = 0$ . Also, no Gibbs oscillation has been observed in the central region of the distribution function where the abrupt jump exists; only in the tails do we find small Gibbs oscillations. This is because the convolution can smear out the discontinuity.

#### 4. Comparison between different collision kernels

It is commonly thought that the solution of the Boltzmann equation is determined by the shear viscosity, rather than the details of the  $\theta$ -dependence of the collision kernel. For instance, the VHS and variable soft sphere models are used in DSMC and it is believed that as long as they recover the shear viscosity of a real gas, they produce the same results [2]. This is true to some extent; one example is the exact BKW solution for Maxwell molecules: different  $\theta$ -dependence of the collision kernels with the same value of shear viscosity have the same BKW solution. However, this assumption has never been accurately checked for other potentials. Since the fast spectral method can generate accurate numerical results, it is interesting to check this assumption. We take the hard sphere ( $\alpha = 1$ ), argon ( $\alpha = 0.38$ ), and soft-potential ( $\alpha = -0.4$ ) molecules as examples. To be specific, we consider the Boltzmann equation (20) with  $Kn = \sqrt{\pi}$  in Eq. (21). The distribution function is given by Eq. (47) with  $t = 0$ . We vary the value of  $\gamma$  and compare the relative error of the collision operator  $Q$ . From Fig. 11, we see that the value of  $\gamma$  has almost no influence on the solution of the collision operator, as the relative errors are at the order of the numerical accuracy (when compared to Maxwell molecules) and seem to be random.

Next we compare the relax-to-equilibrium processes between hard sphere, argon, Maxwell, and soft-potential molecules with  $\gamma = 0$ . The initial distribution function is given by Eq.

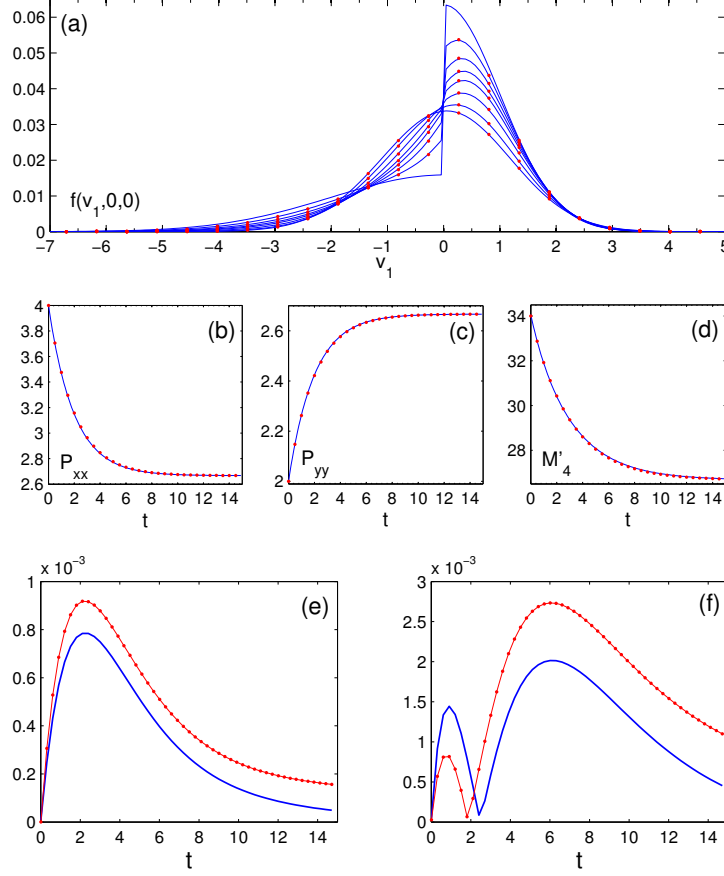


Figure 10: (a) Evolution of the distribution function when the initial distribution function at  $v_1 = +0$  is four times larger than at  $v_1 = -0$ . From top to bottom (at  $v_1 > 0$ ), the times corresponding to each line are  $t = 0, 0.5, 1, 1.5, 2, 3, 5$ , and  $9$ , respectively. (b-d) Evolution of the second- and fourth-order moments. Relative error (e)  $|P_{xx}^{nu} - P_{xx}|/P_{xx}$  and (f)  $|M_4'^{nu} - M_4'|/M_4'$  when  $N = 42$ . The dots are the numerical results when  $N = 42$ , the solid lines in (a), (e), and (f) are the numerical results with  $N_1 = 256, N_2, N_3 = 42$ , while the solid lines in (b-d) are analytical results. Other parameters are  $L = 11$ ,  $R = 2\sqrt{2}L/(3 + \sqrt{2})$ , and  $M = 5$  with Eq. (38).

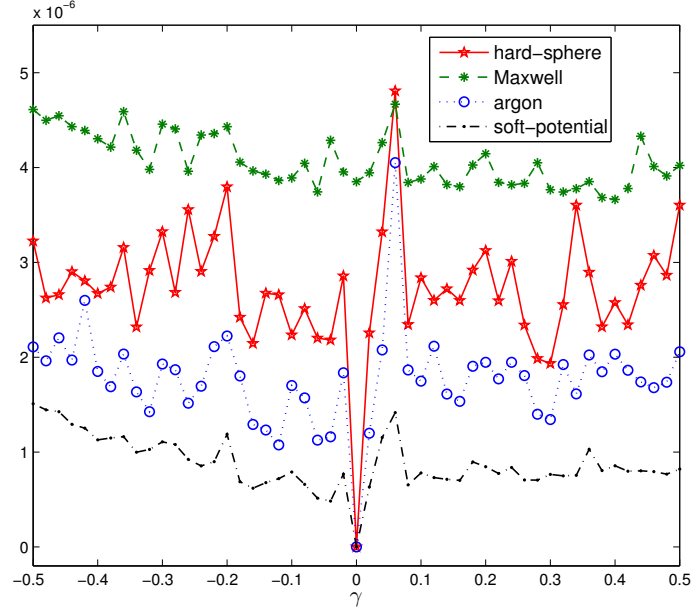


Figure 11: Relative error  $\sum_j |Q_j^{nu} - Q_j^{ref}| / \sum_j |Q_j^{ref}|$  in the approximation of the Boltzmann collision operator vs  $\gamma$ , where  $Q^{ref}$  is the collision term with  $\gamma = 0$  for hard sphere, argon, and soft-potential molecules, while for Maxwell molecules,  $Q^{ref}$  is calculated according to the exact BKW solution. Other parameters are  $L = 8, R = 6, N = 48$ , and  $M = 16$ .

(47) with  $t = 0$ . We choose  $Kn = 2^{1-\omega} \sqrt{\pi}$ , meaning different collision kernels have the same value of shear viscosity at  $T = 2$ . The evolution of the distribution functions are shown in Fig. 12. It is seen that for hard-potential molecules ( $\alpha > 0$ ), in the central velocity region  $[-1, 1]^3$ , the relax-to-equilibrium process is slower than that for Maxwell molecules, and the larger the  $\alpha$ , the slower the decay. In the outer velocity region, however, the decay is faster (although not clearly shown, this can be inferred according to the conservation of mass). For soft-potential molecules ( $\alpha < 0$ ), however, the decay is faster than that for Maxwell molecules in the central velocity region. This may be qualitatively explained in terms of the collision frequency  $\nu(v)$ . From Fig. 13 we see that the collision frequency of hard sphere molecules is smaller (or larger) than that of Maxwell molecules when  $|v| < 4$  (or  $|v| > 4$ ). Therefore, in the central (outer) velocity region, there are less (more) effective collisions between hard sphere molecules than between Maxwell molecules, and hence the decay is slower (faster). Overall, from Fig. 14 we see that, as compared to Maxwell molecules, the competition between the slower and faster decay results in the slower (faster) decay of the fourth- and sixth-order moments for hard-potential (soft-potential) molecules.

The different decay rates between different inverse power-law potential models with the same value of shear viscosity (see Fig. 14) poses a question in the simulation of the LJ potential: since the shear viscosity can be recovered by different combinations of  $\alpha_j$ , we can ask whether different values of  $\alpha_j$  in Eq. (15) lead to different results? To answer this question, we compare the relax-to-equilibrium processes between argon with  $\mu \propto T^{0.81}$  and the LJ potential with the collision kernel (15). The initial distribution function is given by

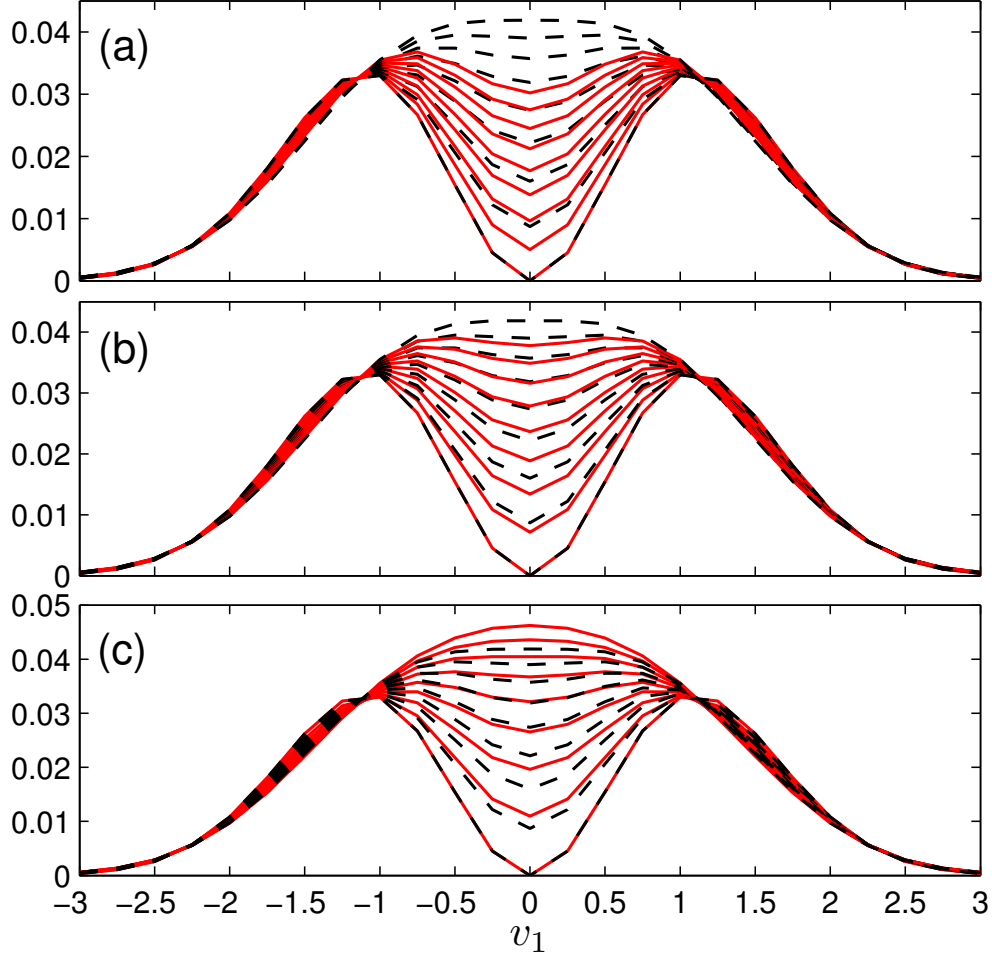


Figure 12: Evolution of the distribution function  $f(v_1, 0, 0)$  for space-homogeneous (a) hard sphere, (b) argon, and (c) soft-potential molecules, where the initial condition is given by Eq. (47). In each figure, from bottom to top (near  $v_1 = 0$ ), the time corresponding to each line is  $(0, 1, 2, 3, 4, 5, 6, 7, 8) \times 0.25$ . The lines are the numerical solutions, and the dashed lines are the analytical solution for Maxwell molecules.

Eq. (47) with  $t = 0$ . For argon, we choose  $Kn = 2^{0.19}\sqrt{\pi}$ , while for the LJ potential we choose  $Kn = 1.0758\sqrt{\pi}$  and  $k_B T_0/\epsilon = 1.1$ , so that the two models have the same value of shear viscosity and for the LJ potential the shear viscosity can be approximated by  $T^{0.81}$  at  $T/T_0 = 2$ . The relative errors in the fourth- and sixth-order moments between the two models are depicted in Fig. 15, where we see that the differences are very small. This example, together with the example shown in Fig. 11, indicate that one can use different  $\theta$ -dependence of the collision kernels as long as the shear viscosity (not only its value, but also its temperature dependence) is recovered.

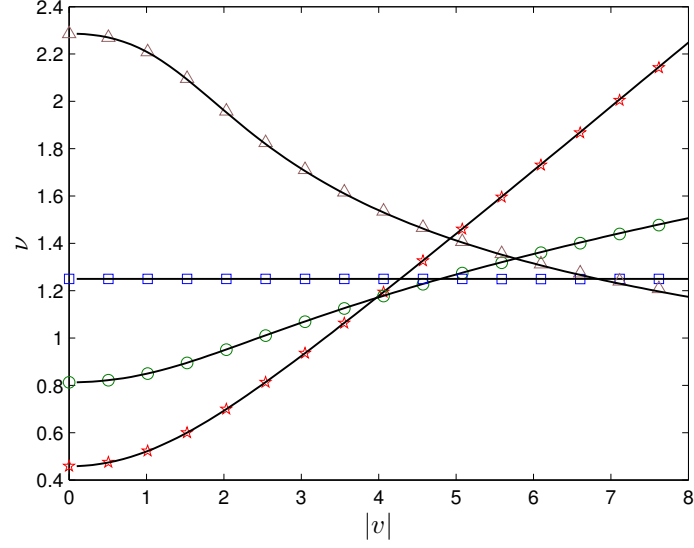


Figure 13: Collision frequency of hard sphere molecules (stars), argon with  $\alpha = 0.38$  (circles), Maxwell molecules (squares), and soft-potential molecules with  $\alpha = -0.4$  (triangles) vs molecular velocity. The lines are analytical results calculated according to equations in Ref. [44]. The distribution function is given by Eq. (47) with  $K = 1$ .

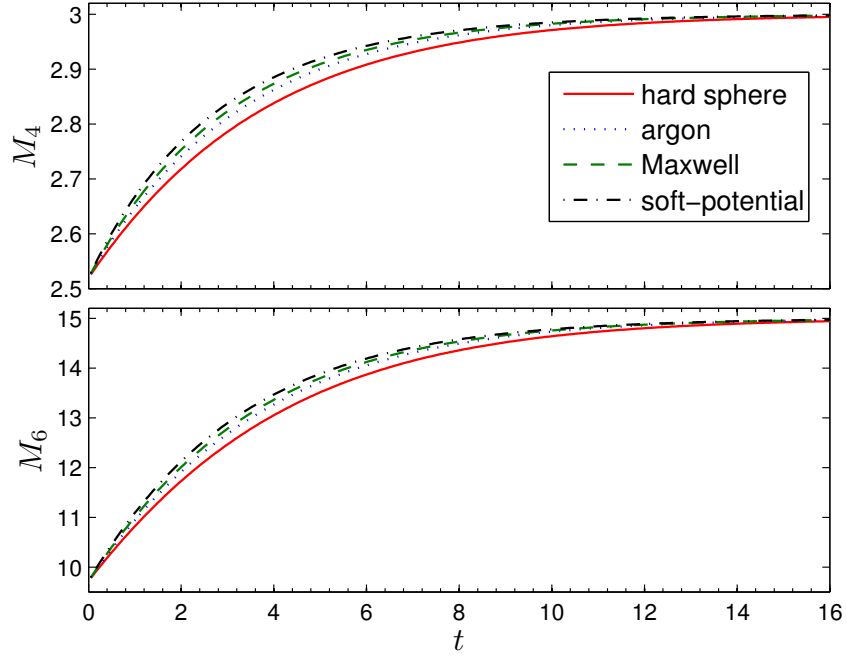


Figure 14: Time evolution of the fourth- and sixth-order moments for various types of collision kernels.

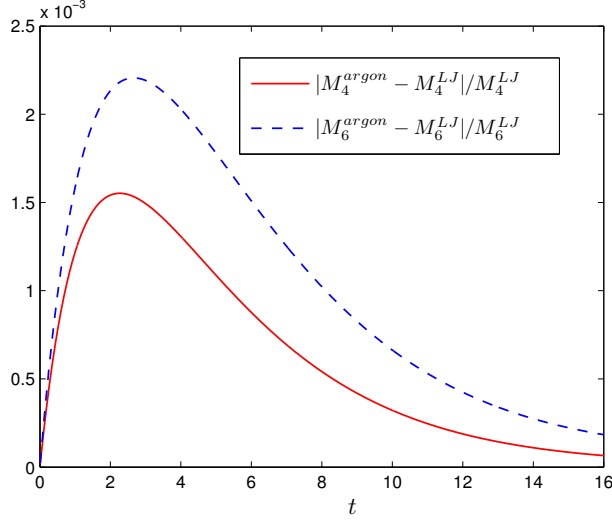


Figure 15: The relative errors in the fourth- and sixth-order moments between argon with  $\mu \propto T^{0.81}$  and the LJ potential with collision kernel (15).

## 5. Numerical solutions for space-inhomogeneous problems

### 5.1. Iteration scheme for spatially-inhomogeneous cases

To get stationary solutions of the Boltzmann equation for space-inhomogeneous problems, the time-dependent term is omitted from the Boltzmann equation, yielding  $v_2 \partial f / \partial x_2 + a_1 \partial f / \partial v_1 = Q(f, f)$ . We then employ the iteration method to solve this equation: given the value of  $f$  at the  $k$ -th step, its value at the next iteration step is calculated by the following equation

$$\bar{\nu} f^{k+1} + v_2 \frac{\partial f^{k+1}}{\partial x_2} = \bar{\nu} f^k - a_1 \frac{\partial f^k}{\partial v_1} + Q(f^k, f^k), \quad (54)$$

where the spatial derivative  $\partial f^{k+1} / \partial x_2$  is approximated by the second-order upwind scheme, and the acceleration term  $a_1 \partial f / \partial v_1$  is calculated according to the Fourier transform derivative theorem, as the velocity distribution function in this direction is smooth. The parameter  $\bar{\nu}$  is a positive constant having the meaning of mean collision frequency, which is introduced to eliminate the singularity in the calculation of Eq. (54) when  $v_2 \simeq 0$ .

The choice of the value of  $\bar{\nu}$  is ad-hoc for space-inhomogeneous problems since different locations have different mean collision frequency, and too large (small) a value of  $\bar{\nu}$  results in slow convergence (numerical instability). A better way is to replace the mean collision frequency by the local collision frequency in the  $k$ -th iteration step, and change  $f^k(v)$  in the loss term  $Q^-$  to  $f^{k+1}(v)$ , yielding

$$\nu(f^k) f^{k+1} + v_2 \frac{\partial f^{k+1}}{\partial x_2} = -a_1 \frac{\partial f^k}{\partial v_1} + Q^+(f^k, f^k). \quad (55)$$

Note that a similar scheme has been used in the study of the structure of shock waves [20, 22]. Also note that in the continuum regime  $Kn \rightarrow 0$  and  $\nu \rightarrow \infty$ , the convergence rate to the

stationary solutions is very slow. In this case, it may be better to solve the time-dependent Boltzmann equation by the asymptotic preserving scheme using relevant larger time step; see the recent review paper [45].

The iteration process is terminated when the maximum  $L_1$  norm of the macroscopic quantities (such as  $n, V, T, P$ , and  $q$ ) at two consecutive iteration steps is less than a fixed small value, say,  $10^{-7}$ . Since there is only a small difference in macroscopic quantities for different values of  $M$ , a trick can be used to reduce the computational cost: we first choose a relatively small value of  $M$ ; when the numerical solution is not far away from the true one we then switch to larger values of  $M$ . In the following calculations, it is found that the use of  $M = 5$  generates satisfactory results. We therefore choose Eq. (38) to approximate the kernel mode (36), since for  $M = 5$  it has almost the same accuracy as that of Gauss-Legendre quadrature but with about 25% increase in computational efficiency.

### 5.2. Accurate calculation of the collision frequency

A problem that remains is how to determine the local collision frequency  $\nu$ . In algorithm 2 we proposed a method. In numerical simulations, however, we find that this method does not give accurate results over the whole velocity range  $[-L, L]^3$ , but only in the region with  $|v| \leq R/\sqrt{2}$ , i.e., the results are accurate within the support of the distribution function. If one is not interested in the distribution function when  $|v| > S$ , the value of  $\nu$  can be fixed for  $|v| > S$  at, say, the value of  $\nu$  at  $|v| \simeq S$ . On the other hand, one can get an accurate collision frequency through enlarging the velocity domain by a factor of two. Details are given in algorithm 3.

Figure 13 depicts the normalized collision frequency  $\nu$  for various kinds of collision kernels when  $Kn = 2^{1-\omega}\sqrt{\pi}$ , and good agreements between the numerical and analytical results are observed. It is seen that the collision frequency of the soft potential for  $|v| \rightarrow 0$  is finite.

### 5.3. Normal shock waves

The normal shock wave is ideal for testing the accuracy of the fast spectral method in capturing highly nonequilibrium effects, since this is a spatially one-dimensional problem where the boundary effects are absent. We first consider the shock wave in a gas of hard sphere molecules. Ohwada solved this problem by means of the finite-difference method [20]. For comparison, we set  $\ell$  to be  $\sqrt{\pi}/2$  times the mean free path of the hard sphere molecules ( $\lambda_0 = (\sqrt{2}\pi d^2 n_0)^{-1}$ ,  $d$  is the diameter of a molecule) and  $Kn' = 8\sqrt{2\pi}$ . Fig. 16 shows the shock wave structure for a Mach number of 3, and it can be seen that the two deterministic numerical methods for the Boltzmann equation give identical results.

We then consider argon with the LJ potential. To compare with experimental data [46], we set the upstream temperature to be  $T_0 = 298$  K,  $\ell = (16/5\pi)\sqrt{\pi/2mk_B T_0}\mu/n_0$  to be the mean free path in the upstream part and  $Kn = 5\pi/16$  in Eq. (23). Good agreement between the numerical and experimental density profiles is seen in Fig. 17. The agreement is due to the fact that we have correctly incorporated the shear viscosity of argon into the collision kernel, shown in Eq. (15).

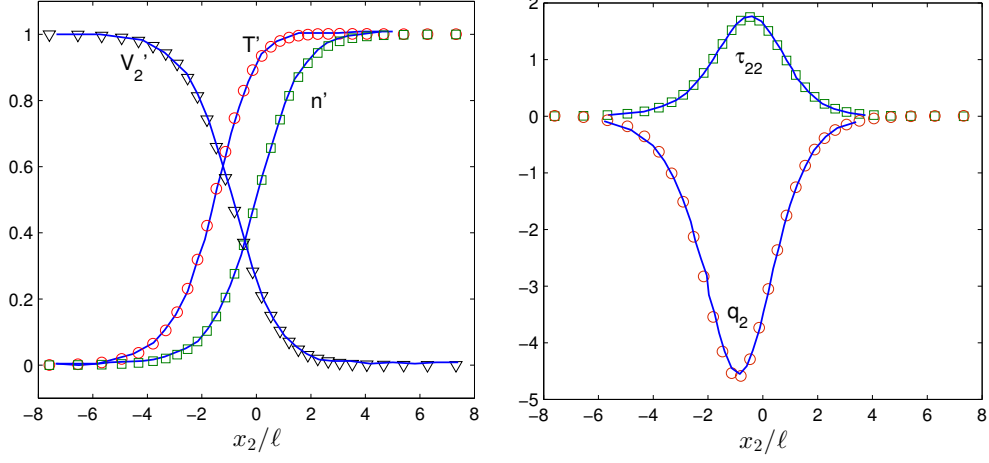


Figure 16: The normal shock wave for  $Ma = 3$ , where the reduced molecular number density is  $n' = (n - 1)/(n_r - 1)$ ; temperature  $T' = (T - 1)/(T_r - 1)$ ; bulk velocity,  $V_2' = (V_2 - V_r)/(\sqrt{5/6}Ma - V_r)$ ; shear stress  $\tau_{22} = P_{22} - nT$ ; and heat flux  $q_2$ . The solid lines are the results from Ref. [20], while the symbols are our results from the fast spectral method. The position of the shock wave is adjusted to  $n'(0) = 1/2$ . The velocity domain  $[-10, 10]^3$  is uniformly divided into  $42 \times 42 \times 42$  grid points, and  $M = 5$ .

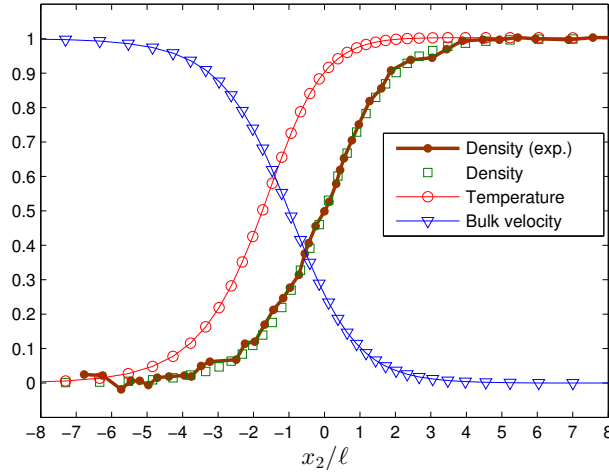


Figure 17: Reduced molecular number density, temperature, and bulk velocity for the normal shock wave for  $Ma = 2.80$ . The experimental density is obtained from Ref. [46]. Numerical parameters are the same as those in Fig. 16.



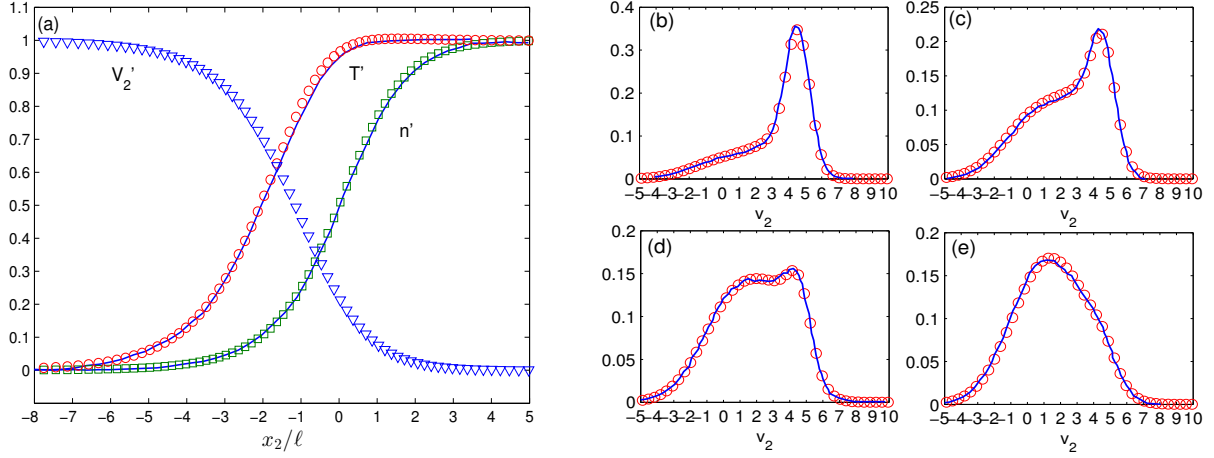


Figure 18: (a) Reduced molecular number density, temperature, and bulk velocity for the normal shock with  $Ma = 5$  in argon gas (LJ potential). The marginal distribution function  $\int \int f dv_1 dv_3 / n$  vs  $v_2$  is presented in (b) at  $n' = 0.151$ , (c)  $n' = 0.350$ , (d)  $n' = 0.511$ , and (e)  $n' = 0.759$ . The solid lines are the results from Ref. [47], while the symbols are our results from the fast spectral method. The velocity domain  $[-18, 18]^3$  is divided into  $42 \times 84 \times 42$  grid points.

Finally, we solve the Boltzmann equation for argon with the LJ potential and compare our results with that of MD simulation [47]. For comparison, we set the upstream temperature to be  $T_0 = 300$  K,  $\ell$  to be the mean free path in the upstream part and  $Kn = 5\pi/16$ . Fig. 18 shows the shock wave structure for Mach number of 5, as well as the parallel distribution functions (the perpendicular distribution functions in Ref. [47] are actually parallel distribution functions). As can be seen from this figure, the fast spectral method produces nearly the same results as the MD simulation. Note that in this case the downstream temperature is about 2600K. The excellent agreement with MD data illustrates that the collision kernel (23) for the LJ potential works well in this temperature range.

#### 5.4. Planar Fourier/Couette/force-driven flows

In planar Couette flow with  $Kn = 1$ , we use argon with a shear viscosity proportional to  $T^{0.81}$ . The wall temperature is  $T_0 = 273$  K, and the wall velocity is  $V_w = \sqrt{2}v_m$  in the first test case and  $V_w = v_m/\sqrt{2}$  in the second one. The spatial region (halved due to the symmetry) is divided into 50 unequally spaced cells, with more cells near the boundary. The maximum velocity is  $L = 8$ , and there are 42 velocity mesh points in each direction. Our numerical results are shown in Fig. 19. In Fig. 20 we show that, when using the iteration scheme given by Eq. (55), the relative error decays exponentially, where, roughly speaking, the characteristic time of decay is inversely proportional to the Knudsen number. The fast spectral method is very efficient when the Mach number is not very large, for instance, in the Couette flow shown in Fig. 19a for which  $Ma \approx 1.5$ , the macroscopic quantities are obtained within 40 seconds (40 iterations, symmetry in the  $v_3$  direction is considered) using our Matlab programme on a PC with an Intel Xeon 3.3 GHz CPU.

In Fourier flow, the temperatures of the lower and upper plates are chosen to be  $T_0 = 273$  K and 373 K, respectively. We consider hard sphere molecules, and  $Kn = 0.5, 1$ , and 5. The

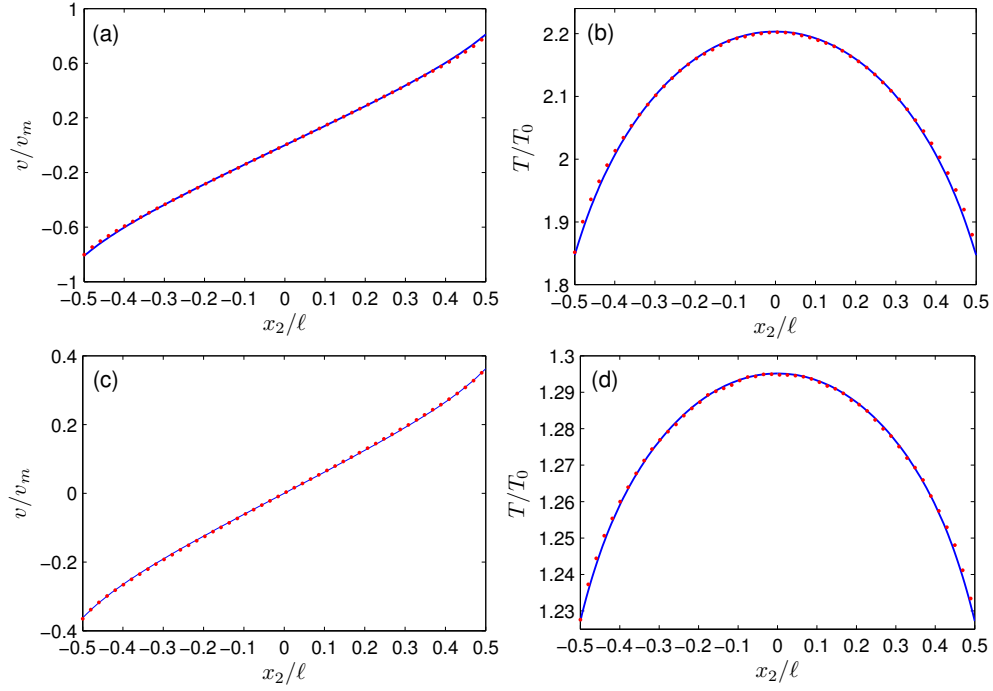


Figure 19: Profiles of normalized velocity and temperature for planar Couette flow of argon gas at  $Kn = 1$ . (a, b)  $V_w = \sqrt{2}v_m$  and (c, d)  $V_w = v_m/\sqrt{2}$ . The solid lines are our numerical results from the fast spectral method, while the dots are DSMC results.

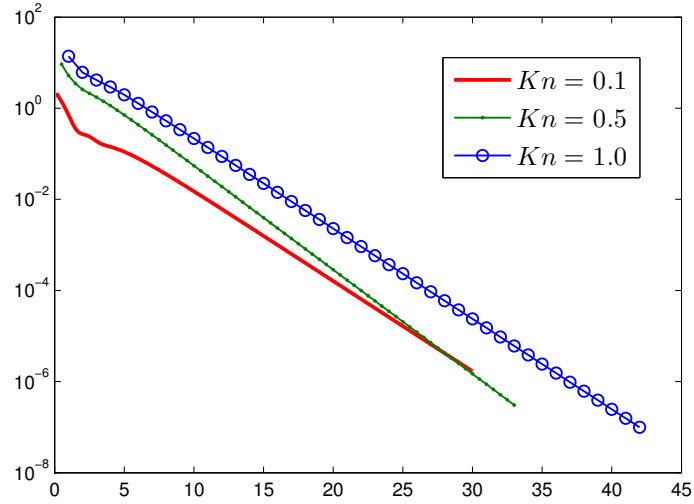


Figure 20: Decay of the relative error in the iteration process. The abscissa is the iteration step times the Knudsen number, while the ordinate is the maximum relative error  $\max(\sum_j |T_j^k - T_j^{k-1}|/T_j^k, \sum_j |n_j^k - n_j^{k-1}|/n_j^k)$ , where  $j$  is the position index.

spatial region is divided into 100 equally spaced cells. The maximum velocity is  $L = 6$ , and there are 32 velocity mesh points in each direction. Comparisons between the fast spectral method and DSMC are summarized in Fig. 21.

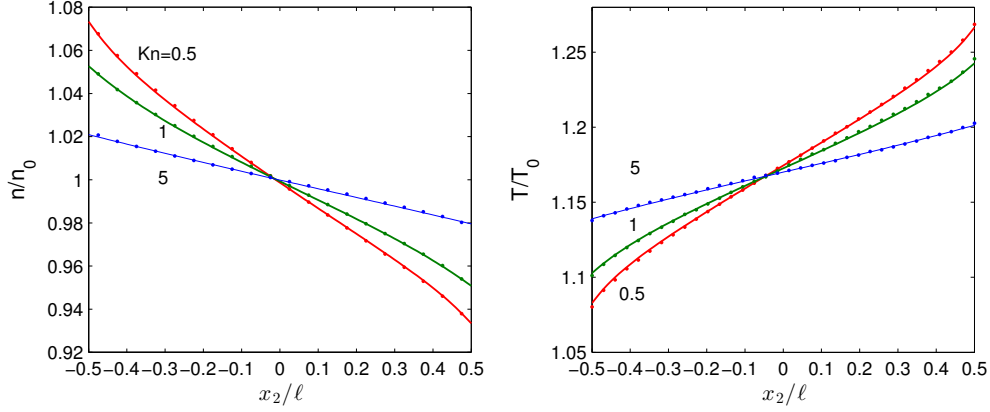


Figure 21: Density and temperature profiles for the planar Fourier flow of hard sphere molecules for unconfined Knudsen numbers of 0.5, 1, and 5. The solid lines are our numerical results from the fast spectral method, while the dots are DSMC results.

In force-driven Poiseuille flow, we use hard sphere molecules and  $Kn = 0.1$  and  $0.5$ . The normalized acceleration is 0.11 and the wall temperature is  $T_0 = 273\text{K}$ . The spatial region (halved due to the symmetry) is divided into 50 unequally spaced cells with more cells near the boundary. The maximum velocity is  $L = 6$ , and there are 32 velocity mesh points in each direction. The numerical results are depicted in Fig. 22.

## 6. Conclusions

The fast spectral method for the approximation of the Boltzmann collision operator has been extended. A modified collision kernel was proposed, which enables the fast spectral method to be applied to all inverse power-law potentials except the Coulomb potential. By appropriate superposition of the modified collision kernels, we recovered the shear viscosity of the Lennard-Jones and rigid attracting potentials. Although many single-term collision kernels are added together, the computational efficiency of the Boltzmann collision operator is still the same as that for the single-term collision kernel. This unique property has advantages over the DSMC technique, where the simulation of soft-potential molecules becomes inefficient because a large number of possible collision pairs are selected but each of which has only a small probability of actually participating in a collision [48]. For the simulation of molecular systems interacting with the Coulomb potential, the following two solutions might be used. The first is to adopt the Fokker-Planck-Landau equation instead of the Boltzmann equation when all the collisions become grazing. For this case, the fast spectral method has already been developed [49]. The second way is to use the Sutherland formula for shear viscosity, where the Boltzmann equation with the collision kernel (17) can be solved by the fast spectral method.

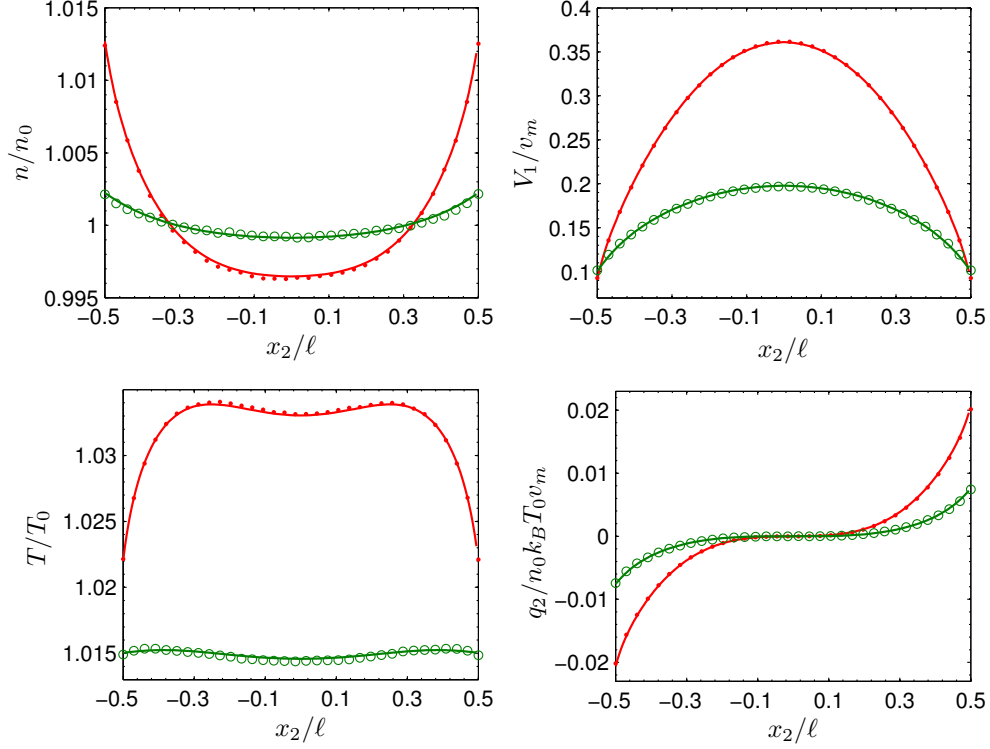


Figure 22: Profiles of normalized number density, velocity, temperature, and heat flux for force-driven Poiseuille flow of hard sphere molecules when  $Kn = 0.1$  (dots) and  $Kn = 0.5$  (open circles). The solid lines are our results from the fast spectral method, the symbols are DSMC results.

The trapezoidal rule and Gauss-Legendre quadrature has been used to approximate the kernel mode. By comparing the numerical solutions with the analytical BKW solutions, we found that the latter is more accurate when  $M > 5$ . When  $M = 5$ , the accuracy is almost the same. We have also found that the spectrally small errors in the momentum and energy in the fast spectral method can be eliminated by using the Lagrangian multiplier method, while spectral accuracy is retained.

With accurate solutions provided by the fast spectral method, we checked whether the solution of the Boltzmann equation is affected by the  $\theta$ -dependence of the collision kernel or not. Within the numerical accuracy (relative errors are about  $10^{-6}$ ) we found that, for the same inverse power-law potential with the same value of shear viscosity but different forms of the  $\theta$ -dependence of the collision kernel, the solutions to the Boltzmann equation are the same. This justifies the fact that one can use different forms of the collision kernel so long as the shear viscosity (not only its value, but also its temperature dependence) is recovered.

The fast spectral method has also been applied to space-inhomogeneous problems, including the normal shock wave and planar Fourier/Couette/force-driven Poiseuille flows. Our numerical results are found to agree well with those of a finite-difference solution to the Boltzmann equation, experimental data, and MD and DSMC solutions.

Since the fast spectral method solves the Boltzmann equation deterministically, it is use-

ful for developing a hybrid solver, where in the continuum regime kinetic models (or Navier-Stokes equations) are used, while in the rarefied regime the Boltzmann equation is solved. The open question remains as to how to determine the location of the continuum/rarefied interface.

The dealiasing condition requires the velocity domain to be about two times larger than the support of the distribution function, which wastes more than half of the compute memory and time in three-dimensional velocity space. A better way to do this is to introduce the non-uniform FFT [50], where the velocity space is non-uniformly discretized but the frequency space is equally divided. The only change we need is to get the spectrum  $\hat{f}$  from  $f$  and the collision operator  $Q$  from  $\hat{Q}$  by non-uniform FFTs, while the FFT-based convolution remains unchanged. Since the main computational effort is devoted to the calculation of FFT-based convolution, the non-uniform FFT will not increase the computation time much, especially when many efficient non-uniform FFT algorithms are available. Therefore, the use of fewer non-uniform velocity mesh points (with most of the points lying in the support of the distribution function) will need less compute memory and time, without sacrificing of accuracy.

The fast spectral method is also ready to be extended to mixtures of monatomic molecules. For hard sphere molecules, one can use the collision kernel (11), while for other cases, one should use the modified collision kernel (13) and choose special values of  $\gamma$  to recover the correct coefficients of shear viscosity and diffusion.

## Acknowledgements

The authors thank the referees for their valuable suggestions.

## Appendix A. Algorithm 1: calculation of the collision operator

```

step 1.    $\hat{f} = \text{FFTSHIFT}\{\text{IFFT}[\text{FFTSHIFT}(f)]\}$ 
step 2.    $\hat{Q}^+ = 0$ 
           For  $\theta_p = (1, 2, \dots, M-1)\pi/M$ 
             For  $\varphi_q = (1, 2, \dots, M)\pi/M$ 
                $t_1 = \hat{f} \cdot \phi_{\alpha+\gamma}(\xi_l, \theta_p, \varphi_q)$ 
                $t_2 = \hat{f} \cdot \psi_\gamma(\xi_m, \theta_p, \varphi_q)$ 
               zero-padding  $t_1, t_2$  to the dimension  $\geq \frac{3N_1}{2} \times \frac{3N_2}{2} \times \frac{3N_3}{2}$ 
                $\hat{Q}^+ = \hat{Q}^+ + \text{FFT}(t_1) \cdot \text{FFT}(t_2) \cdot \sin \theta_p$ 
             End
           End
step 3.    $t_1 = \hat{f}$ 
            $t_2 = \hat{f} \cdot \phi_{loss}$ 
           zero-padding  $t_1, t_2$  to the dimension  $\geq \frac{3N_1}{2} \times \frac{3N_2}{2} \times \frac{3N_3}{2}$ 
            $\hat{Q}^- = \text{FFT}(t_1) \cdot \text{FFT}(t_2)$ 
step 4.    $\hat{Q} = \text{IFFT}(\hat{Q}^+ - \hat{Q}^-)$ 
           delete the redundant data in  $\hat{Q}$ 
step 5.    $Q = (4\pi^2/\text{Kn}' M^2) \text{FFTSHIFT}\{\Re[\text{FFT}[\text{FFTSHIFT}(\hat{Q})]]\}$ 

```

**Note.** FFTSHIFT represents the Matlab function that shifts the zero-frequency component to the center of spectrum, IFFT is the inverse FFT, and the function  $\Re$  gets the real parts of complex numbers.

## Appendix B. Algorithm 2: simpler and faster calculation of the collision operator

```

step 1.    $\hat{f} = \text{FFTSHIFT}\{\text{IFFT}[\text{FFTSHIFT}(f)]\}$ 
step 2.    $Q^+ = 0$ 
             For  $\theta_p = (1, 2, \dots, M-1)\pi/M$ 
               For  $\varphi_q = (1, 2, \dots, M)\pi/M$ 
                  $Q^+ = Q^+ + \text{FFT}[\hat{f} \cdot \phi_{\alpha+\gamma}(\xi_l, \theta_p, \varphi_q)] \cdot \text{FFT}[\hat{f} \cdot \psi_\gamma(\xi_m, \theta_p, \varphi_q)] \cdot \sin \theta_p$ 
               End
             End
              $Q^+ = (4\pi^2/\text{Kn}' M^2) \text{FFTSHIFT}[\Re(Q^+)]$ 
step 3.    $\nu = (4\pi^2/\text{Kn}' M^2) \text{FFTSHIFT}\{\Re[\text{IFFT}[\text{FFTSHIFT}(\hat{f} \cdot \phi_{\text{loss}})]]\}$ 
              $Q^- = \nu f$ 
step 4.    $Q = Q^+ - Q^-$ 
Note. Here  $\nu = \int \int \sin^{\alpha+\gamma-1}(\theta/2) \cos^{-\gamma}(\theta/2) |u|^\alpha [f(v_*)] d\Omega dv_*/Kn'$  is the normalized collision frequency, which is accurate when the velocity is within the support of the distribution function, i.e.,  $|v| \leq R/\sqrt{2}$ .

```

## Appendix C. Algorithm 3: accurate calculation of the collision frequency

```

step 1.   calculate  $\phi_{\text{loss}}^{\text{ex}}$  according to Eq. (42) with  $L^{\text{ex}} = 2L$  and  $R^{\text{ex}} = \sqrt{2}L$ 
step 2.   create a zero-value array  $f^{\text{ex}}$  of size  $2N_1 \times 2N_2 \times 2N_3$ 
step 3.   copy the value of  $f$  to the middle of  $f^{\text{ex}}$ 
step 4.    $\hat{f}^{\text{ex}} = \text{FFTSHIFT}\{\text{IFFT}[\text{FFTSHIFT}(f^{\text{ex}})]\}$ 
step 5.    $\nu^{\text{ex}} = (4\pi^2/\text{Kn}' M^2) \text{FFTSHIFT}\{\Re[\text{IFFT}[\text{FFTSHIFT}(\hat{f}^{\text{ex}} \cdot \phi_{\text{loss}}^{\text{ex}})]]\}$ 
step 6.   copy the middle region value of  $\nu^{\text{ex}}$  to  $\nu$ .

```

## References

- [1] S. Chapman and T. G. Cowling, *The Mathematical Theory of Non-uniform Gases*, Cambridge University, Cambridge, 1970.
- [2] G. A. Bird, *Molecular Gas Dynamics and the Direct Simulation of Gas Flows*, Clarendon Press, Oxford, 1994.
- [3] K. Nanbu, Direct simulation scheme derived from the Boltzmann equation. I. Monocomponent gases, *J. Phys. Soc. Japan*, 52 (1983) 2042-2049.
- [4] W. Wagner, A convergence proof for Bird's direct simulation Monte Carlo method for the Boltzmann equation, *Journal of Statistic Physics* 66 (1992) 1011-1044.
- [5] Q. H. Sun, I. D. Boyd, G. V. Boyd, A hybrid continuum/particle approach for micro-scale gas flows, *Rar. Gas. Dynam.* 663 (2003)
- [6] T. E. Schwartzentruber, L. C. Scalabrin, and I. D. Boyd, A modular particle-continuum numerical method for hypersonic non-equilibrium gas flows, *J. Comput. Phys.* 225 (2007) 1159-1174.
- [7] J. M. Burt and I. D. Boyd, A hybrid particle approach for continuum and rarefied flow simulation, *J. Comput. Phys.* 228 (2009) 460-475.
- [8] G. Dimarco and L. Pareschi, Hybrid multiscale methods. II. Kinetic equations, *Multiscale. Model. Simul.* 6 (2008) 1169-1197.
- [9] L. L. Baker and N.G. Hadjiconstantinou, Variance reduction for Monte Carlo solutions of the Boltzmann equation, *Physics of Fluids*, 17 (2005) 051703.
- [10] T. M. M. Homolle and N.G. Hadjiconstantinou, A low-variance deviational simulation Monte Carlo for the Boltzmann equation, *J. Comput. Phys.* 226 (2007) 2341-2358.
- [11] D. Goldstein, B. Sturtevant, and J. E. Broadwell, Investigations of the motion of discrete-velocity gases, *Rar. Gas. Dynam. Progress in Aeronautics and Astronautics*. 118, AIAA, Washington, 1989.
- [12] A. V. Bobylev, A. Palczewski, and J. Schneider, On approximation of the Boltzmann equation by discrete velocity models, *C. R. Acad. Sci. Paris* 320 (1995) 639-644.
- [13] V. V. Aristov and F. G. Tcheremissine, Direct numerical solutions of the kinetic Boltzmann equation, *Comp. Center of Russ. Acad. of Sci. Moscow*, 1992.
- [14] W. Wagner, Approximation of the Boltzmann equation by discrete velocity models, *J. Statist. Phys.* 78 (1995) 1555-1570.
- [15] C. Buet, A discrete-velocity scheme for the Boltzmann operator of rarefied gas dynamics, *Transport Theory Statist. Phys.* 25 (1996) 33-60.
- [16] A. B. Morris, P. L. Varghese, and D. B. Goldstein, Improvement of a discrete velocity Boltzmann equation solver that allows for arbitrary post-collision velocities, in: *Rarefied Gas Dynamics: Proceedings of the 26th International Symposium*, Kyoto, Japan, 2008.
- [17] A. B. Morris, P. L. Varghese, and D. B. Goldstein, Monte Carlo solution of the Boltzmann equation via a discrete velocity model, *J. Comput. Phys.* 230 (2011) 1265-1280.
- [18] C. Mouhot, L. Pareschi, and T. Rey, Convolutional decomposition and fast summation methods for discrete-velocity approximations of the boltzmann equation, *arXiv:1201.3986v1*.
- [19] Y. Sone, T. Ohwada, and K. Aoki, Temperature jump and Knudsen layer in a rarefied gas over a plane wall: Numerical analysis of the linearized Boltzmann equation for hard-sphere molecules, *Phys. Fluids A* 1 (1989) 363-370.
- [20] T. Ohwada, Structure of normal shock waves: Direct numerical analysis of the Boltzmann equation for hard-sphere molecules, *Phys. Fluids* 5 (1993) 217-234.
- [21] T. Ohwada, Heat flow and temperature and density distributions in a rarefied gas between parallel plates with different temperatures. Finite-difference analysis of the nonlinear Boltzmann equation for hard-sphere molecules, *Phys. Fluids* 8 (1996) 2153-2160.
- [22] S. Kosuge, K. Aoki, and S. Takata, Shock-wave structure for a binary gas mixture: finite-difference analysis of the Boltzmann equation for hard-sphere molecules, *Eur. J. Mech. B/Fluids* 20 (2001) 87-126.
- [23] A. V. Bobylev, The theory of the nonlinear spatially uniform Boltzmann equation for Maxwell molecules, *Mathematical Physics Reviews* 7 (1988) 111-233.



- [24] L. Pareschi and B. Perthame, A Fourier spectral method for homogeneous Boltzmann equation, *Transport Theory Statist. Phys.* 25 (1996) 369-382.
- [25] A. V. Bobylev and S. Rjasanow, Difference scheme for the Boltzmann equation based on fast Fourier transformation, *Eur. J. Mech. B/Fluids* 16 (1997) 293-306.
- [26] C. Watchararuangwita, Y. N. Grigoriev, and S. V. Meleshko, A deterministic spectral method for solving the Boltzmann equation for one-dimensional flows, *ScienceAsia* 35 (2009) 70-79.
- [27] A. V. Bobylev and S. Rjasanow, Fast deterministic method of solving the Boltzmann equation for hard spheres, *Eur. J. Mech. B/Fluids* 18 (1999) 869-887.
- [28] I. Ibragimov and S. Rjasanow, Numerical solution of the Boltzmann equation on the uniform grid, *Computing* 69 (2002) 163-186.
- [29] I. M. Gamba and S. H. Tharkabhushanam, Spectral-Lagrangian methods for collisional models of non-equilibrium statistical states, *J. Comput. Phys.* 228 (2009) 2012-2036.
- [30] I. M. Gamba and S. H. Tharkabhushanam, Shock and boundary structure formation by spectral-Lagrangian methods for the inhomogeneous Boltzmann Transport Equation, *J. Comp. Math.* 28 (2010) 430-460.
- [31] L. Pareschi and G. Russo, Numerical solution of the Boltzmann equation I: Spectrally accurate approximation of the collision operator, *SIAM J. Numer. Anal.* 37 (2000) 1217-1245.
- [32] F. Filbet and G. Russo, High order numerical methods for the space non-homogeneous Boltzmann equation, *J. Comput. Phys.* 186 (2003) 457-480.
- [33] C. Mouhot and L. Pareschi, Fast algorithms for computing the Boltzmann collision operator, *Math. Comput.* 75 (2006) 1833-1852.
- [34] F. Filbet, C. Mouhot, and L. Pareschi, Solving the Boltzmann equation in  $N \log_2 N$ , *SIAM J. Sci. Comput.* 28 (2006) 1029.
- [35] F. Filbet, On deterministic approximation of the Boltzmann equation in a bounded domain, *Multiscale Modeling and Simulation* 10 (2012) 792-817.
- [36] F. Filbet, J. Hu, and S. Jin, A numerical scheme for the quantum Boltzmann equation with stiff collision terms, *Math. Model. Num. Anal.* 46 (2012) 443-463.
- [37] J. Hu and L. Ying, A fast spectral algorithm for the quantum Boltzmann collision operator, *Commun. Math. Sci.* 10 (2012) 989.
- [38] P. T. Gressman and R. M. Strain, Global classical solutions of the Boltzmann equation with long-range interactions, *Proceedings of the National Academy of Sciences*, 107 (2010) 5744.
- [39] H. A. Hassan and D. B. Hash, A generalized hard-sphere model for Monte Carlo simulation, *Phys. Fluids A* 5 (1993) 738.
- [40] H. Matsumoto, Variable sphere molecular model for inverse power law and Lennard-Jones potentials in Monte Carlo simulations, *Phys. Fluids* 14 (2002) 4256.
- [41] J. Fan, Generalized soft-sphere model for Monte Carlo simulation, *Phys. Fluids* 14 (2002) 4399.
- [42] C. Canuto, M. Y. Hussaini, A. Quarteroni, and T. A. Zang, *Spectral Methods in Fluid Dynamics*, Springer-Verlag, New York, 1988.
- [43] M. Krook and T. T. Wu, Exact solutions of the Boltzmann equation, *Phys. Fluids* 20 (1977) 1589.
- [44] H. Struchtrup, *Macroscopic transport equations for rarefied gas flows: approximation methods in kinetic theory interaction of mechanics and mathematics*, page 44, 1st edn. Heidelberg, Germany: Springer, 2005.
- [45] L. Pareschi and G. Russo, Efficient asymptotic preserving deterministic methods for the Boltzmann equation, AVT-194 RTO AVT/VKI, Models and Computational Methods for Rarefied Flows, Lecture Series held at the von Karman Institute, Rhode St. Genese, Belgium, 24-28 January (2011).
- [46] P. Kowalczyk, A. Palczewski, G. Russo, and Z. Walenta, Numerical solutions of the Boltzmann equation: comparison of different algorithms, *Eur. J. Mech. B/Fluids* 27 (2008) 62-74.
- [47] P. Valentini and T. E. Schwartzentruber, Large-scale molecular dynamics simulations of normal shock waves in dilute argon, *Phys. Fluids* 21 (2009) 066101.
- [48] M. N. Macrossan and C. R. Lilley, Modified generalized hard sphere collision model for direct simulation Monte Carlo calculations, *J Thermophys Heat Transfer* 17 (2003) 289-291.

- [49] L. Pareschi, G. Russo, and G. Toscani, Fast Spectral Methods for the Fokker-Planck-Landau Collision Operator, *J. Comput. Phys.* 165 (2000) 216-236.
- [50] A. Heintz, P. Kowalczyk, and R. Grzibovskis, Fast numerical method for the Boltzmann equation on non-uniform grids, *J. Comput. Phys.* 227 (2008) 6681-6695.